Modulation of F-actin dynamics by maternal Mid1ip1L controls germ plasm aggregation and furrow recruitment in the zebrafish embryo

Eno, C., Pelegri, F.

Laboratory of Genetics, University of Wisconsin – Madison

Corresponding author: fjpelegri@wisc.edu

Keywords: Mid1ip1L, germ plasm, ribonucleoparticles, microtubules, F-actin, zebrafish, embryo

Abstract

During the early embryonic cell cycles, zebrafish germ plasm ribonucleoparticles (RNPs) gradually multimerize and become recruited to the forming furrows. RNPs multimerization occurs prior to and during furrow initiation, as forming aggregates move outward through their association with the tips of growing interphase astral microtubules. Germ plasm RNPs are also associated with short cortical F-actin. We show that, in embryos mutant for the cytoskeletal regulator *mid1ip1L*, germ plasm RNPs fail to become recruited to the furrow, accumulating instead at the periphery of the blastodisc. RNP aggregates are associated with zones of *mid1ip1L*-dependent cyclical local cortical F-actin network enrichments as well as contractions at both the cortex and the contractile ring. F-actin inhibition in wild-type embryos mimics the RNP peripheral accumulation defect of *mid1ip1L* mutants. Our studies suggest that a common mechanism underlies distinct steps of germ plasm RNP segregation. At the cortex, this process attenuates microtubule-dependent outward RNP movement to retain RNPs in the blastodisc cortex and allow their recruitment to the furrows. F-actin network contraction likely also facilitates higher order germ plasm RNP multimerization.

Introduction

In many animal species, including the zebrafish *Danio rerio*, primordial germ cell specification occurs through the inheritance of the so-called germ plasm, a maternally-derived specialized cytoplasm containing specific RNAs and proteins (Wylie, 1999; Strome and Lehmann, 2007; Eno and Pelegri, 2013). In the zebrafish, germ plasm ribonucleoparticles (RNPs) accumulate at the cleavage furrows for first two embryonic cell divisions to generate four large aggregates (Yoon et al., 1997; Pelegri et al., 1999; Knaut et al., 2000). As blastomeres fully cellularize, these aggregates become incorporated into primordial germ cells (Olsen et al., 1997; Yoon et al., 1997; Braat et al., 1999, Knaut et al., 2000). Removal of the cytoplasm in the region harboring the germ plasm results in embryos lacking primordial germ cells (Hashimoto et al., 2004), as do treatments that interfere with germ plasm segregation (Miranda-Rodríguez et al., 2017). Conversely, an increase in germ plasm aggregates results in excess germ cells (Bontems et al., 2009).

Immediately after fertilization, germ plasm RNPs are relatively evenly dispersed through the blastodisc (Theusch et al., 2006), with RNPs appearing under fluorescence microscopy as single spherical units of typically less than a micron in diameter (Eno and Pelegri, 2013; Nair et al., 2013; this study). The assembly of germ plasm masses during the first embryonic cell cycles involves sequential steps in which RNPs, while appearing to remain as distinct units, multimerize to form increasingly larger aggregates (Fig. 1).

An initial step, “pre-aggregation”, occurs in the blastodisc cortex even prior to furrow formation, resulting in multimers, or pre-aggregates, consisting of a small number of RNPs (typically < 20; Nair et al., 2013). During pre-aggregation, RNPs are cleared from the center of the blastodisc while a wave-front of RNP multimers forms at the inner edge of the surrounding RNP-containing

band (Theusch et al., 2006; Nair et al., 2013). Previous analysis suggests that the outwardly RNP clearing and associated RNP multimerization wave-front is driven by sperm aster and mitotic spindle astral microtubules (Theusch et al., 2006; Nair et al., 2013), which undergo radially outward growth (Wühr et al., 2010) and whose tips are associated with germ plasm RNPs (Nair et al., 2013). Function of Birc5b (a.k.a. Motley), a maternal-specific duplicate product for the Chromosomal Passenger Complex (CPC) Survivin, has been shown to be a necessary link between astral microtubule ends and the germ plasm aggregate (Nair et al., 2013)

A second step, "furrow recruitment", occurs as early blastomeres undergo cytokinesis and involves the local gathering of RNPs to the forming furrow through the action of astral microtubules originating from opposite sides of the mitotic spindle (Wühr et al., 2010; Nair et al., 2013) and maternal kinesin-1 motor protein Kif5Ba function (Campbell et al., 2015). This generates elongated, rod-like arrangements of aggregates along the base of the furrow, altogether involving a large number of RNPs (ca. 500-1000 for furrows corresponding to the first two cell cycles; Eno and Pelegri, 2013). A third step, "distal compaction", occurs as the furrow matures and involves the transition of the set of aggregates distributed along the furrow base into a single compact mass at each of the furrow distal ends (Pelegri et al., 1999; Eno and Pelegri, 2013).

The steps of RNP pre-aggregation, furrow recruitment and distal compaction are reitiretated through the early embryonic cycles, allowing for the systematic gathering of germ plasm RNPs into multiple germ plasm masses (Eno and Pelegri, 2013). The largest four masses, those that form at the furrows for the first and second cell cycle, subsequently become incorporated into primordial germ cells. This work focuses on F-actin-dependent mechanisms underlying multimerization and movement during these three stages of germ plasm segregation. The

accompanying article (Eno et al., submitted) addresses cues mediating the directional movement of the forming germ plasm mass towards furrow distal ends during the distal compaction stage.

In addition to their attachment to microtubule ends, during their multimerization and movement germ plasm RNPs are associated with short F-actin fragments (Theusch et al., 2006; Nair et al., 2013). Similar to germ plasm RNPs, cortical F-actin undergoes a gradual microtubule-dependent movement towards the blastodisc periphery, where it accumulates forming circumferential arcs composed of short F-actin (Theusch et al., 2006; Nair et al., 2013). The close association of F-actin fragments to RNPs during their multimerization and outward movement suggests F-actin is involved in one or both of these processes.

We recently reported that the maternal-effect gene *aura* encodes the cytoskeletal regulator Mid1ip1L and is required for the reorganization of cortical F-actin in the early embryo, including the formation of circumferential arcs (Eno et al., 2016). Here, we show that, in *aura* mutant embryos, germ plasm RNP aggregates fail to become recruited to the forming furrow, instead accumulating in peripheral regions of the blastodisc. This phenotype is associated with an accelerated rate of outward RNP movement in mutants. Inhibition of the F-actin network mimics, and stabilization of F-actin partially rescues, the *aura* mutant germ plasm segregation phenotype, suggesting that dynamics events within the F-actin cortex regulate germ plasm RNP movement. *aura/mid1ip1L* function is required for the generation of cyclical patterns of dynamic cortical F-actin enrichment as well as cortical trench-like contractions corresponding to circumferential F-actin arcs. *aura/mid1ip1L*-dependent F-actin local contractions are also observed at the contractile band during furrow formation, where they are also associated with RNP aggregate fusion. Our studies indicate that regulated *aura/mid1ip1L*-dependent cortical F-actin dynamics mediates germ plasm segregation prior to and during furrow formation.

Materials and Methods

Fish maintenance and genetic methods

Fish stocks were raised and maintained under standard conditions at 28.5° (Brand et al., 2002). All animals were handled in strict accordance with good animal practice as defined by the relevant national and/or local animal welfare bodies, and all animal work was approved by the appropriate committee (University of Wisconsin-Madison assurance number A3368–01). Wild-type stocks were AB and *mid1ip1L* mutants included both *aura*^{t9792} (Pelegri et al., 2004) and *mid1ip1L*^{uw39} (Eno et al., 2016). Fish were identified either through their phenotype or genotypic typing using custom-designed LNA probes (IDT) to distinguish mutant from wild-type via end-point genotyping on a Roche LC480 qPCR system (Table S1). For embryo collection and synchronization, fish were mated and embryos collected within a 5 min interval during mating.

Immunofluorescence and in situ hybridization

For immunofluorescence detection, embryos were dechorionated using pronase, and fixed in 4% paraformaldehyde, 0.25% glutaraldehyde, 5mM EGTA, 0.2% Triton X-100 and 0.2 U/ml Rhodamine (or Alexa-488)-conjugated phalloidin for 3-5 hrs at RT. Embryos were treated with 0.5 mg/ml $NaBH_4$, washed with PBS-T (Triton-X 0.1%), blocked with PBST + 10% BSA for 1 hr at RT (Theusch et al., 2006), and incubated ON with primary antibodies: p-NMII (1:50: CST, 3710) and Mid1ip1L (1:200, Antibodies Online). Embryos were incubated with secondary antibodies against mouse or rabbit conjugated to Alexa 488 (1:200, Thermofisher) or Cy3 (1:200, Jackson Immuno Labs) and rhodamine-phalloidin (1:200, Cytoskeleton) or Alexa-488-phalloidin (1:200, Thermofisher).

For fluorescent in situ hybridization, embryos were fixed with 4% PFA while still in their chorions. Fixed embryos were labeled using a fluorescein-labeled antisense RNA probe for the gene *vasa* (Yoon et al., 1997) and detected using the Fluorescein system (Perkin Elmer) following "Triple fluorescent in situ" protocol (modified Talbot protocol, ZFIN). For all immunofluorescent and *in situ* experiments, the embryos were de-yolked after labeling, stained with DAPI (Theusch et al., 2006) and the blastodiscs were mounted flat on slides for imaging. Percent of recruitment presented is based on the number of furrows, typically 2-4 per embryo imaged. Embryos were imaged using a Zeiss LSM510 for confocal or 780 for structured illumination microscopy and analyzed using FIJI, including 3D Viewer.

Live Imaging

Both wild-type and *aura* (Eno et al., 2016) embryos carrying the Life Act (Tg(actb2:LIFEACT-GFP)) (Behrndt et al., 2012) transgene were dechorionated and placed in glass bottom microscopy slide (Ibidi) in E3. Embryos laying animal pole side down were imaged on an inverted Zeiss LSM780. Images were taken every 2 s at 100x magnification with 2x digital zoom. 3-D rendering, projections, movies, montages and kymographs were generated using FIJI.

Drug exposure

Wild-type and *aur*^{t9792} embryos were dechorionated using pronase (Pelegri and Schulte-Merker, 1999) and exposed to the drug in E3 by 15 mpf. Concentrations of inhibitors in E3 medium: cytochalasin D (Thermofisher), 20 µg/ml; phalloidin (P3457), 10 µg/ml; nocodazole (Sigma), 2 µg/ml; and taxol (Sigma), 10 µg/ml. Control for drug treatment were solutions carrying the same concentration of carrier solvent (DMSO).

Results

Mutations in the maternal gene *aura/mid1ip1L* lead to failed germ plasm RNP furrow recruitment

As previously reported (Yoon et al., 1997; Pelegri et al., 1999; Theusch et al., 2006; Eno and Pelegri, 2013) germ plasm RNPs present in the blastocyst cortex of wild-type embryos, such as those containing *vasa* RNA, form a characteristic rod-like structure along the forming furrows for the first two mitotic cycles (35 mpf; Fig. 2A,A'; 96%, n=45). Previous studies have shown that maternal homozygosity for mutations in *aura/mid1ip1L* leads to defects in the early embryo including in cortical granule release and the completion of cytokinesis, defects that invariably result in embryonic lethality (Pelegri et al., 2004; Eno et al., 2016). However, using molecular markers, we find that, in embryos from females homozygous for mutations in *aura/mid1ip1L*, animal germ plasm RNPs fail to localize to the forming furrow (Figs. 2B,B', S1), accumulating instead as aberrantly large aggregates at the periphery of the blastodisc (Fig. 2B, bracket; 11% with furrow localization, n=45). This phenotype is observed in embryos from females homozygous for either the mutant allele aur^{t9792} allele (Fig. 2, S1), which deletes a conserved C-terminal domain in the Mid1ip1L protein (Eno et al., 2016), or the CRISPR/Cas9-induced allele aur^{uw39} (Fig. S2), which deletes most of the Mid1ip1L protein and is therefore presumed to be a null allele (Eno et al., 2016). For simplicity, we refer to embryos from *aura/mid1ip1L* homozygous mutant females as *aura/mid1ip1L* mutant embryos.

aura/mid1ip1L mutant embryos exhibit defects in furrow formation, but these defects occur at late stages of cytokinesis (45-55 mpf). On the other hand, furrow initiation in *aura/mid1ip1L* mutants at earlier stages (30-40 mpf), a time coincident with the observed defect in animal germ

plasm RNP furrow recruitment, is largely normal (Eno et al., 2016). Thus, the RNP recruitment phenotype observed in *aura/mid1ip1L* mutants is likely caused by cellular events that occur prior to and during furrow initiation, independent of the late cytokinesis defects.

Germ plasm RNP aggregation is associated with cortical F-actin surface trenches

Because *aura/mid1ip1L* mutants exhibit defects in cortical F-actin dynamics even prior to furrow formation (Eno et al., 2016), and since animal germ plasm RNPs are associated with cortical F-actin (Theusch et al., 2006; Nair et al., 2013), we explored whether the RNP furrow recruitment phenotype in *aura/mid1ip1L* mutants is related to cortical F-actin defects. For these experiments, and in order to increase sensitivity and preserve subcellular morphology, we took advantage of the ability of anti-P-myosin monoclonal antibody to label most germ plasm RNAs in the 1- to 4-cell stage embryo (Nair et al., 2013). Our previous studies have shown that wild-type embryos form cortical F-actin arcs, composed of short F-actin fragments, that run along the periphery of the blastodisc (Theusch et al., 2006; Nair et al., 2013; Eno et al., 2016) (Figs. 3A, 4A-D). *aura/mid1ip1L* mutants, on the other hand, exhibit reduced formation of circumferential F-actin arcs (Eno et al., 2016) (Figs. 3B, 4E-H). Orthogonal views of these projections reveal that the F-actin arcs found in wild-type correspond to trench-like indentations at the cortex (Fig. 3A',A"). Such cortical trenches are often associated in their cytoplasmic side with RNP aggregates (Fig. 3A'). In *aura/mid1ip1L* mutants, although RNPs appear associated with cortical F-actin, the F-actin cortex appears as a flat surface lacking cortical trenches (Fig. 3B',B").

aura/mid1ip1L mutants show an increased outward germ plasm RNP movement along the blastodisc cortex

In a time course analysis of fixed samples, cortical F-actin and associated germ plasm RNPs are initially distributed throughout most of the blastodisc (Fig. 4A,A'), and show the expected outward movement during sperm aster formation immediately prior to and during the first several cell divisions (Theusch et al., 2006; Nair et al., 2013; Fig. 4B-D, white double arrows denote RNP domain). In *aura* mutant embryos, the initial distribution and number of RNPs appears normal compared to wild-type (Figs. 4E; S3). However, concomitant with the cortical F-actin reorganization defect, RNP pre-aggregates accumulate to the distal edge of the blastodisc at a rate that appears to be faster than wild type (Fig. 4F-H). We quantified the rate of outward movement of cortical RNPs by determining the ratio of the RNP-free domain, from the center of the blastodisc to the RNP aggregation front (at the inner rim of the RNP peripheral band (red double arrows)) relative to the radius of the blastodisc. This analysis shows a significantly increased outward movement of the germ plasm RNP aggregation front in mutants (Fig. 4I).

F-actin dynamics modulates microtubule-dependent outward movement of germ plasm RNPs

Given the role of *aura/mid1ipL* in cortical F-actin dynamics (Eno et al., 2016), we tested the effect of F-actin inhibitors and stabilizers on germ plasm RNP furrow recruitment in embryos co-labeled for the germ plasm marker P-myosin and F-actin (Fig. 5), assaying at a time when in control wild-type embryos RNPs have become recruited to the furrows for the first two cycles (60 mpf, 84% of furrows with large aggregates, n=50) and a fraction of RNPs remains associated with F-actin arcs at the blastodisc margin (Eno and Pelegri, 2013; Nair et al., 2013; Fig. 5A).

Treatment of wild-type embryos with the F-actin inhibitor cytochalasin D results in a reduced fraction of furrows with germ plasm RNP furrow recruitment (30%, n=20), defects similar to those observed in control *aura/mid1ip1L* mutants (25%, n=20). In cytochalasin D-treated wild-type embryos, cortical F-actin arcs fail to form and RNP aggregates are found mostly as large aggregates at the outer periphery of the blastodisc (Fig. 5B), again reminiscent of the *aura/mid1ip1L* mutant phenotype (Fig. 5E). Cytochalasin D treatment of *aura/mid1ip1L* mutants results in an apparent enhancement of the F-actin and RNP segregation phenotype (0% furrow recruitment, n=8), with RNPs accumulating at the margin (Fig. 5F). Treatment of wild-type embryos with the F-actin stabilizer phalloidin does not have a significant effect on RNP furrow localization (90%, n=20) and does not affect F-actin arc formation nor lead to ectopic marginal RNP aggregates (Fig. 5C). However, phalloidin treatment restores RNP furrow recruitment in *aura/mid1ip1L* mutants (95%, n=20), allowing F-actin arc formation and reducing ectopic marginal RNP aggregates (Fig. 5G). Similar effects on germ plasm RNP segregation were obtained when visualizing germ plasm with a probe to detect *dead end* RNA (Weidinger et al., 2003) using in situ hybridization (Fig. S4). Quantification of the position of the RNP aggregation front at 60 mpf shows that inhibition of the F-actin network results in an increase in the extent of outward RNP movement (95.4%, n=9; Fig. 5I) compared to control wild-type (70.3%, n=13), similar to the increase observed in *aura/mid1ip1L* mutant embryos (93.0%, n=7, see also Fig. 4). These results suggest that Mid1ip1L-dependent cortical F-actin dynamics functions in the modulation of outward clearing of germ plasm RNP segregation, leading to furrow recruitment.

As expected (Theusch et al., 2006; Nair et al., 2013), treatment of wild-type embryos with the microtubule depolymerizing agent nocodazole results in germ plasm RNPs being distributed in more central regions of the cortex due to a reduced degree of outward movement of RNP

aggregates (29.1% RNP clearance from blastodisc center, n=13, compared to 80.9% in control wild-type, n=4; Fig. 5D,J). In *aura/mid1ipL* mutants, nocodazole treatment also results in decreased outward RNP clearance (53.3%, n=10, compared to 91.3% in control mutants, n=4; Fig. 5J), and reverses the ectopic marginal accumulation of RNP aggregates (Fig. 5H). Thus, the formation of peripheral ectopic aggregates in *aura/mid1ip1L* mutants, as in wild-type (Theusch et al., 2006; Nair et al., 2013), is dependent on microtubule-dependent outward RNP movement.

Altogether, these data suggest that the Mid1ip1L function and the F-actin network are required to attenuate microtubule-dependent outward movement of cortical germ plasm RNPs, and that this modulation is necessary for their recruitment to the furrows.

Cortical F-actin exhibits *aura/mid1ip1L*-dependent cyclical enrichment

To investigate further the dynamic nature of cortical F-actin and its dependence on Mid1ip1L, we carried out live imaging of actin in wild-type and mutant embryos using a LifeAct transgene (Behrndt et al., 2012). In wild-type early embryos before first furrow formation (between 15-30 mpf), cortical F-actin exhibits repeated cycles of F-actin enrichments (Fig. 6A, white and red circles; Movie 1). These F-actin enrichments appear to reappear in the same location with a periodicity of about 80 sec, in a manner reminiscent of previously described cyclical cortical F-actin polymerization patterns in the *Xenopus* and starfish oocytes and early embryonic cells (Bement et al., 2015). *aura* mutant embryos do not show these cyclical patterns, exhibiting instead a relatively static network that gradually reorganizes into punctate circular patterns similar to those observed in fixed samples (Fig. 6B,D,D'; Movie 2; see also Eno et al., 2016). F-actin ring-like structures, though smaller and not as punctate or frequently observed as in

aura/mid1ip1L mutants, can also be discerned amidst cortical F-actin enrichments in wild-type embryos (Fig. 6C,C'). Kymograph analysis from live imaging data shows that in wild-type cortical F-actin exhibits a characteristic undulating pattern through time, involving slight lateral shifts of F-actin enrichment (Fig. 6C"). In contrast, in *aura* mutants localized cortical F-actin enrichments do not undergo lateral shifts, remaining instead in a static pattern that dissipates over time (Fig. 6D"). As expected from the analysis of fixed samples, wild-type embryos treated with cytochalasin D exhibit reduced and dynamic F-actin networks, respectively (Movies 3 and 4), and phalloidin treatment partially rescues F-actin dynamics in live *aura/mid1ip1L* mutants (Movie 5).

aura/mid1ip1L is required for F-actin cortical waves associated with germ plasm RNP aggregates

3-D rendered orthogonal views of the cortical F-actin cytoskeleton show key differences between wild-type and mutant embryos as well as embryos treated with cytoskeletal inhibitors (Fig. 7). Wild-type embryos show cortical trenches (Fig. 7A, corresponding to Fig. 3A'), whereas these structures are entirely lacking in *aura/mid1ip1L* mutants (Fig. 7G, corresponding to Fig. 3B') or cytochalasin D-treated wild-type embryos (Fig. 7C). Although phalloidin-treated wild-type embryos did not exhibit a statistically significant increase in cortical trenches (Fig. 7E), phalloidin treatment caused a significant increase in cortical F-actin trench formation in *aura/mid1ip1L* mutants compared to control-treated mutant embryos (Fig. 7I, quantification in K), consistent with a rescuing effect through F-actin stabilization of the phenotypes associated with *aura/mid1ip1L* mutations (Eno et al., 2016). Thus, Mid1ip1L function is required for the

formation of cortical F-actin trench-like structures associated with germ plasm RNP pre-aggregates.

Shared *aura/mid1ip1L*-dependent features at the cortex and furrows associated with germ plasm RNP aggregation

Remarkably, a pattern of repeated wave-like structures was also observed in optical cross-sections of F-actin at the furrow, with wild-type furrows showing repeated indentations (Fig. 7B). Similar to the case for the F-actin cortex, these indentations are not present in *aura* mutants (Fig. 7H). Also similar to cortical F-actin trench formation (Fig. 7C), cytochalasin treatment of wild-type embryos results in furrow F-actin without indentations (Fig. 7D), mimicking the *aura* mutant phenotype. Moreover, and also reminiscent of the effect on cortical trenches (Fig. 7I), phalloidin treatment restores the ability of furrow F-actin to form indentations in *aura/mid1ip1L* mutant embryos (Fig. 7J, quantification in L). In addition, F-actin accumulations at the furrow as seen in a face on (animal) view, corresponding to furrow indentations, appear continuous with F-actin enrichments at the abutting cortex, corresponding to cortical trenches (Fig. S5). Thus, these two types of F-actin structures, cortical trenches and furrow indentations, are induced by a functionally related Mid1ip1L-dependent mechanism and are structurally linked.

As with the case of surface contraction trenches at the cortex (Fig. 8A-C, see also Fig. 3A'), F-actin indentations at the furrow are associated with germ plasm RNP aggregates (Fig. 8D-F, which appear to be in close association with, and typically in between, furrow indentations (Fig. 8G,G'). In cases in which the RNP aggregate at the furrow is a relatively elongated structure, it is

often observed to be associated via one of its ends to the furrow indentation, with most of the aggregate mass protruding into the cytoplasm (Fig. 8G').

Notably, cortical trenches and furrow indentations exhibit a directional accumulation over time. Cortical trenches span a progressively reduced and more distal location of the blastodisc in a radial direction (Fig. 8A-C,A'-C', quantified in H) mirroring the outward movement of the germ plasm RNP aggregation front. Furrow indentations also occur in a progressively more distally confined region, in this case in a medial-to-distal direction along the furrow (Fig. 8D-F,D'-F', quantified in I), mirroring the compaction of the RNP aggregate.

The directional tightening of F-actin cortical trenches and furrow indentations is consistent with a role in their gradual encroachment of RNP aggregates to facilitate their fusion into increasingly larger aggregates, which eventually accumulate at the furrow distal ends. Indeed, RNPs can be observed as streams of single particles in between adjacent aggregates at the furrow (Fig. 8G, G"), a behavior consistent with inter-aggregate fusion. Thus, wild-type embryos exhibit *aura/mid1ip1L*-dependent wave-like contractions at the cortex and furrows, which in both cases are associated with germ plasm RNP aggregates and appear to regulate their movement and aggregation.

Mid1ip1L associates with dynamic cortical F-actin

We used Structured Illumination Microscopy (SIM) to visualize Mid1ip1L protein in relation to cortical F-actin with increased resolution compared to previous studies (Eno et al., 2016). In control wild-type embryos, Mid1ip1L protein largely co-localizes with cortical F-actin (Fig. 9A), as well as in F-actin enrichments regions at the furrow (Fig. 9B). Interestingly, Mid1ip1L protein

and F-actin do not fully colocalize, revealing regions within or immediately adjacent to F-actin enrichments that contain higher levels of Mid1ip1L protein, and viceversa. In mutants for the *aura*^{t9792} allele, which lacks the majority of the protein except for a conserved C-terminal domain, Mid1ip1L protein is present, but the localization to actin is drastically reduced (Eno et al., 2016; data not shown).

Interfering with F-actin polymerization with cytochalasin D treatment results in the expected reduction in cortical F-actin. Under this condition, Mid1ip1L protein appears highly punctate, showing reduced overlap to any remaining cortical F-actin (Fig. S6B). Treatment of wild-type embryos with phalloidin also results in an apparently reduced degree of localization between Mid1ip1L protein and F-actin (Fig. S6C). In contrast to treatments that affect F-actin dynamics, embryos treated with the microtubule inhibitor nocodazole do not exhibit apparent differences in the pattern of colocalization of Mid1ip1L protein and F-actin observed in control wild-type embryos (Fig. S6D). Thus, Mid1ip1L protein binds specific regions of short cortical F-actin, and this binding depends on F-actin dynamics (see Discussion).

Discussion

Previous studies have shown that zebrafish germ plasm RNPs are associated with cortical F-actin, and that microtubule growth mediates the movement of RNPs associated with the actin network, which results in RNP multimerization and localization to the furrows (Theusch et al., 2006; Nair et al., 2013). Here, we show that dynamic reorganization of the cortex, mediated by the function of maternal Mid1ip1L, is required to retain RNPs to the cortex during the early

cleavage cycles in order to allow their recruitment to the forming furrows. Surprisingly, *mid1ip1L*-dependent F-actin dynamic mechanisms appear conserved at both the early embryo cortex and furrows, showing shared mechanisms associated with germ plasm RNP movement and multimerization prior to and during furrow formation.

Mid1ip1L-dependent germ plasm RNP cortical retention is essential for furrow recruitment

Zebrafish germ plasm is inherited in the egg as RNPs associated with the animal cortex of the early zygote (Theusch et al., 2006; Nair et al., 2013; segregation of a subset of germ plasm RNPs, localized to the vegetal pole, is discussed in Theusch et al., 2006; Eno and Pelegri, 2016). Association of these animal germ plasm RNPs to the plus ends of astral microtubules during early embryonic development results in their outward movement, with aggregates forming along what appear to be outwardly moving aggregation waves at the inner rim of an RNP cortical band. Soon after fertilization, germ plasm RNPs appear associated with short F-actin seeds, with the CPC protein Birc5b acting as necessary link between the ends of growing astral microtubules and a complex involving RNPs and F-actin (Nair et al., 2013). RNP recruitment during cell division depends on their gathering at the furrow from adjacent cortical regions, mediated by the action of interphase astral microtubules (Eno and Pelegri, 2013; Nair et al., 2013).

Aided by a process of internal priming (Ishihara et al., 2014), interphase astral microtubules appear to reach the outermost regions of the blastodisc and forming blastomeres, (Wühr et al., 2009; Wühr et al., 2010), an ability that allows for furrow induction in large, dividing blastomeres (Yabe et al., 2009). We find that ectopic localization of RNP aggregates to the blastodisc periphery in *aura/mid1ip1L* mutant embryos correlates with an increased rate of

outward movement of the RNP aggregation front in the embryo, and that inhibition of cortical actin results in similar effects. These observations suggest a modulatory function for Mid1ip1L and cortical F-actin to reduce the rate of outward RNP movement. In wild-type, the attenuation of germ plasm RNP peripheral movement by Mid1ip1L function and cortical F-actin allows cortical RNPs to be partially retained in the blastodisc cortex, where astral microtubules for the following cell cycle can promote further RNP furrow recruitment (Fig. 10, wild-type (WT)). In the absence of this attenuation, as in *aura/mid1ip1L* mutants, outward forces bring RNPs prematurely to the blastodisc periphery, rather than to the furrow (Fig. 10, *aura*). Thus, our studies suggest that the rate of germ plasm RNP aggregate outward movement is finely regulated in order to balance two opposing forces, microtubule-dependent outward RNP movement, which promotes their collection at the furrow plane by bipolar spindles during cell division, and Mid1ipL-dependent RNP retention at the cortex, which allows for the gradual collection of RNPs in furrow planes during consecutive cell cycles.

The end result of this process is the formation of four large germ plasm masses, one at each furrow end for the first and second cell cycles (Eno and Pelegri, 2013). Cell cleavage orientation in the zebrafish embryo is specified independently of the axis of dorsal induction (Abdelilah and Driever, 1997). We speculate that the location of these germ plasm masses, which generate primordial germ cells in all four quadrants of the embryo, maximize the potential to populate the gonad through mechanisms of chemokine-guided cell migration (Paksa and Raz, 2015).

Mid1ip1L-dependent F-actin dynamics and surface wave formation

We find that wild-type embryos exhibit cycles of Mid1ip1L-dependent cortical F-actin polymerization and depolymerization. We additionally find the presence of F-actin indentations at the cortex, also dependent on Mid1ip1L function, which corresponds to previously described circumferential F-actin bands (Theusch et al., 2006; Nair et al., 2013). We do not yet know the precise interconnection between F-actin polymerization cycling, observed in cortices of live embryos, and the formation of cortical F-actin bands and trenches observed in fixed samples. However, both of these events are dependent on Mid1ip1L function and we observe in live embryo cortices F-actin alignment, albeit only partial, reminiscent of F-actin bands in fixed embryos (Fig. 6A). It is also possible that fixation arrests cycles of cortical contraction at a specific point in the F-actin cycle, highlighting the elongated circumferential trenches that can be observed in fixed samples. In addition to a potential connection to cortical contraction formation (see below), Mid1ip1L-dependent lateral cortical movement may help accelerate RNP-RNP encounters and therefore multimerization of single RNPs into the observed pre-aggregates.

Some of the processes we observe in zebrafish may be conserved, as *Xenopus* germ plasm aggregation has been found to depend on surface contraction waves at the vegetal pole of the embryos (Savage and Danilchik, 1993). Moreover, cortical F-actin in *Xenopus* and starfish oocytes and early embryonic cells exhibits Rho-dependent cycles of polymerization and depolymerization that initiate at anaphase onset, leading to cytokinesis (Bement et al., 2015). The latter are similar to those we observe in the zebrafish embryo, although in *Xenopus* and starfish these cycles occur independently of the segregation of germ cell determinants, which are restricted to the vegetal pole in these species (Whittington and Dixon, 1975; Ressom and Dixon,

1988; Savage and Danilchik, 1993; Juliano et al, 2010). It is possible that the early zebrafish embryo has coopted an already existing cortical process to precisely regulate germ plasm segregation.

Super-resolution images shows that Mid1ip1L localizes to the ends of short F-actin, a localization that is reduced by both inhibition of actin polymerization with cytochalasin D and F-actin stabilization with phalloidin. Similar to the effect on germ plasm RNP segregation, defects in cortical contractions in *aura/mid1ip1L* mutants are mimicked by F-actin depolymerization and partially rescued by F-actin stabilization (see also Eno and Pelegri, 2016). Considering these findings, we envision that Mid1ip1L protein either promotes F-actin polymerization at its plus (barbed) end (Fig. S7, top), of negatively regulates F-actin depolymerization at its minus (pointed) end (Fig. S7, bottom). Stabilization of F-actin with phalloidin may allow for proper filament length in *aura* mutant embryos, and the formation of surface contractions (Fig. S7), although additional defects in *aura* mutants such as in internal membrane recycling (Eno et al 2016) and furrow maturation (Eno et al., 2016; Eno et al., 2018) likely preclude the ability of phalloidin to fully rescue the *aura* cytokinesis defect (Eno et al, 2016; our unpublished data).

Several possible mechanisms may allow Mid1ip1L-dependent F-actin dynamics to produce cortical trenches, including F-actin ruffling (Ballestrem et al., 1998), polymerization coupled to membrane attachment (Nawaz et al., 2015; Zuchero et al., 2015), F-actin flow (Comrie et al., 2015) or actomyosin contraction (Schaefer et al., 2002; Burnette et al., 2011). Mid1ip1L protein, initially identified as an interacting factor of the X-linked causal gene for Opitz G/BBB syndrome in humans (Quaderi et al., 1997; Gaudenz et al., 1998; Cox et al., 2000; De Falco et al., 2003; Winter et al., 2003), does not contain obvious functional motifs to explain these

interactions, although the protein has been shown to regulate both microtubules (Berti et al., 2004) and F-actin (Eno et al., 2016).

The periodic nature of the observed trenches is intriguing. In motile cells, while treadmilling is constitutive during F-actin ruffling, ruffles only appear at certain points (Ballestrem et al., 1998). Similarly, F-actin hotspots accumulate periodically where F-actin undergoes continues assembly and disassembly (Ganguly et al., 2015). In the latter system F-actin accumulation occurs at 3-4 microns apart, a distance similar to that between F-actin arcs in the early zebrafish embryo. It will be interesting to determine how apparently constitutive mechanisms determine the observed periodic patterns of cortical F-actin.

Further work will also be required to understand how Mid1ip1L-dependent F-actin dynamics and cortical indentations attenuate the outward movement of germ plasm RNPs. Previous studies suggest dynamic actin and actomyosin contractility can actively influence cell surface molecules to form transient clusters (Goswami et al., 2008; Gowrishankar et al., 2012) and can alter diffusion of GPI-anchored cortical proteins (Saha et al., 2015). Competitive binding of germ plasm RNPs between microtubule tips and F-actin (Alberico et al., 2016; Mohan and John, 2016; Cabrales-Fontela et al., 2017), as RNPs move outwardly through the action of astral microtubule growth, may also explain the modulation of RNP movement by the actin network.

During the early cell cycles in the zebrafish embryo, intracellular components undergo active redistribution through ooplasmic streaming, a process that depends on F-actin function (Roosen-Runge, 1938; Kane and Kimmel, 1993; Leung et al., 2000; Fernández et al., 2006; Fuentes and Fernández, 2010; Li-Villarreal et al., 2015). We can not rule out scenarios in which Mid1ip1L- and F-actin-mediated RNP retention occurs indirectly through the modulation of cytoplasmic flow. However, the bulk of ooplasmic streaming into the blastodisc occurs through internal yolk

cell channels, likely generating a central-to-peripheral flow in the blastodisc (see, for example (Li-Villarreal et al., 2015). Such a flow would be unlikely to contribute to RNP retention, which we infer occurs in the opposite direction. In addition, we observe RNP aggregates only in cortical locations (Theusch et al., 2006; Eno and Pelegri, 2013; Nair et al.. 2013; this report), and not in internal regions if these were to cycle through cytoplasmic streams.

Parallel Mid1ip1L-dependent mechanisms in the blastodisc cortex and the furrow

Surprisingly, we found indentations in furrow F-actin that share similarities to trenches found in the blastodisc cortex. In both cases, these indentations are Mid1ip1L-dependent and are affected by inhibitors of F-actin dynamics. Trenches and indentations exhibit an apparent movement towards more peripheral regions of the blastodisc (outwardly for cortical trenches and medial-to-distal for furrow indentations). These similarities strongly suggest similar underlying mechanisms drive F-actin deformations at both the cortex and the furrow.

The directionality of inferred movement suggests the involvement of traveling F-actin waves (t-waves; Allard and Mogilner, 2013), which may be responding to different signals at the cortex compared to the furrow. At the cortex, outward directionality may be caused by the growth of interphase astral microtubules, whereas at the furrow, medial-to-distal directionality may be conferred by furrow-associated directional cues (see accompanying manuscript Eno et al.).

An encroachment mechanism for germ plasm RNP aggregation

Germ plasm has been proposed to generate a fluid phase different from that of the cytoplasm in various systems (Brangwynne et al., 2009; Updike et al., 2011; Wang et al., 2014; Nott et al., 2015), including the zebrafish (Riemer et al., 2015), which by virtue of differential affinity may

promote particle-particle binding. An increase in particle density is expected to facilitate particle encounters whose different properties may cause particle-particle adhesion. Outward movement of germ plasm RNPs linked to growing astral microtubules result in an increase in RNP relative density that likely facilitates inter-particle encounters.

We find an association of germ plasm RNP aggregates with cortical F-actin trenches at the blastodisc cortex, as well as F-actin indentations at the furrow, with RNP aggregates connected to the cytoplasmic side of the trench/indentation. Considering this association, the gradual convergence of indentations and trenches (into peripheral blastodisc cortex and distal furrow regions, respectively) likely acts to gradually encroach RNP aggregates, increasing RNP density and promoting multimerization. Indeed, we observe instances in which adjacent RNP aggregates appear to have particles streaming from one aggregate to another, consistent with the fluid phase character of the aggregates, and which may constitute intermediate stages in the aggregate fusion process.

Our work shows that Mid1ip1L-dependent cortical F-actin dynamics and deformations regulate the movement of germ plasm RNPs, allowing their recruitment to the forming furrows and likely facilitating RNP multimerization. These events occur through an intrinsic Mid1ip1L-dependent mechanism that is modified by successive extrinsic polarity signals, first radially outward on the cortex, and subsequently medial-to-distally along the furrow. These processes constitute sequential steps that facilitate the movement and aggregation of germ plasm RNPs in the early embryo.

Acknowledgments

We thank members of our laboratory for advice during various stages of this work, as well as animal husbandry staff for the care of the aquatic facility. We thank Erica Weber for her assistance with imaging analysis. Funding was provided by NIH grants to C.C.E (GM108449) and F.P. (GM065303).

References

Abdelilah, S. and Driever, W. (1997). Pattern formation in *janus*-mutant zebrafish embryos. *Dev. Biol.* **184**, 70-84.

Alberico, E. O., Z. C. Zhu, Y.-F. O. Wu, M. K. Gardner, D. R. Kovar and Goodson, H. V. (2016). Interactions between the microtubule binding protein EB1 and F-actin. *J. Mol. Biol.* **428**, 1304-1314.

Allard, J. and Mogilner, A. (2013). Traveling waves in actin dynamics and cell motility. Curr. *Opin. Cell Biol.* **25**, 107-115.

Ballestrem, C., B. Wehrle-Haller and Imhof, B. A. (1998). Actin dynamics in living mammalian cells. *J. Cell Sci.* **111**, 1649-1658.

Behrndt, M., G. Salbreux, P. Campinho, R. Hauschild, F. Oswald, J. Roensch, S. W. Grill and Heisenberg, C.-P. (2012). Forces driving epithelial spreading in zebrafish gastrulation. *Science* **338**, 257-260.

Bement, W. M., M. Leda, A. M. Moe, A. M. Kita, M. E. Larson, A. E. Golding, C. Pfeuti, K. C. Su, A. L. Miller, A. B. Goryachev and Von Dassow, G. (2015). Activator-inhibitor coupling between Rho signalling and actin assembly makes the cell cortex an excitable medium. *Nat. Cell Biol.* **17**, 1471-1483.

Berti, C., B. Fontanella, F. Ferrentino and Meroni, G. (2004). Mig12, a novel Opitz syndrome gene product partner, is expressed in the embryonic ventral midline and co-operates with Mid1 to bundle and stabilize microtubules. *BMC Cell Biol.* **5**, 9.

Bontems, F., A. Stein, F. Marlow, J. Lyautey, T. Gupta, M. C. Mullins and Dosch, R. (2009). Bucky ball organizes germ plasm assembly in zebrafish. *Curr. Biol.* **19**, 414-422.

Braat, A. K., T. Zandbergen, S. van de Water, H. J. T. Goos and Zivkovic, D. (1999). Characterization of zebrafish primordial germ cells: morphology and early distribution of vasa RNA. *Dev. Dyn.* **216**, 153-167.

Brand, M., M. Granato and Nüsslein-Volhard, C. (2002). Keeping and raising zebrafish. In *Zebrafish - A Practical Approach*, Vol. 261 (ed. C. Nüsslein-Volhard and R. Dahm), pp.7-37. Oxford: Oxford University Press.

Brangwynne, C. P., C. R. Eckmann, D. S. Courson, A. Rybarska, C. Howege, J. Gharakhani, F. Jülicher and Hyman, A. A. (2009). Germline P granules are liquid droplets that localize by controlled dissolution/condensation. *Science* **324**, 1729-1732.

Burnette, D. T., S. Manley, P. Sengupta, R. Sougrat, M. W. Davidson, B. Kachar and Lippincott-Schwartz, J. (2011). A role for actin arcs in the leading edge advance of migrating cells. *Nat. Cell Biol.* **13**, 371-381.

Cabrales-Fontela, Y., H. Kadavath, J. Biernat, D. Riedel, E. Mandelkow and Zweckstetter, M. (2017). Multivalent cross-linking of actin filaments and microtubules through the microtubule-associated protein Tau. *Nat. Comm.* **8**, 1981.

Campbell, P.D., A.E. Heim, M.Z. Smith, and Marlow, F.L. (2015) Kinesin-1 interacts with Bucky ball to form germ cells and is required to pattern the zebrafish body axis. *Development* **142,** 2996-3008.

Comrie, W. A., A. Babich and Burkhardt, J.K. (2015). F-actin flow drives affinity maturation and spatial organization of LFA-1 at the immunological synapse. *J. Cell Biol.* **208**, 475-491.

Cox, T. C., L. R. Allen, L. L. Cox, B. Hopwood, B. Goodwin, E. Haan and Suthers, G. K. (2000). New mutations in MID1 provide support for loss of function as the cause of X-linked Opitz syndrome. *Hum. Mol. Genet.* **9**, 2553-2562.

De Falco, F., S. Cainarca, G. Andolfi, R. Ferrentino, C. Berti, G. Rodríguez Criado, O. Rittinger, N. Dennis, S. Odent, A. Rastogi, J. Liebelt, D. Chitayat, R. Winter, H. Jawanda, A. Ballabio, B. Franco and Meroni, G. (2003). X-linked Opitz syndrome: novel mutations in the *MID1* gene and redefinition of the clinical spectrum. *Am. J. Hum. Genet.* **120A**, 222-228.
Eno, C. and Pelegri, F. (2013). Gradual recruitment and selective clearing generate germ plasm aggregates in the zebrafish embryo. *Bioarchitecture* **3**, 125-132.
Eno, C. and Pelegri, F. (2016). Germ cell determinant transmission, segregation and function in the zebrafish embryo. In *Insights from animal reproduction* (ed. R. P. Carreira), pp. 115-142. Rijeka, Croatia: InTech.
Eno, C., B. Solanki and Pelegri, F. (2016). *aura (mid1ip1l)* regulates the cytoskeleton at the zebrafish egg-to-embryo transition. *Development* **143**, 1585-1599.
Fernández, J., M. Valladares, R. Fuentes and Ubilla, A. (2006). Reorganization of cytoplasm in the zebrafish oocyte and egg during early steps of ooplasmic segregation. *Dev. Dyn.* **235**, 656-671.
Fuentes, R. and Fernández, J. (2010). Ooplasmic segregation in the zebrafish zygote and early embryo: pattern of ooplasmic movements and transport pathways. *Dev. Dyn.* **239**, 2172-2189.
Ganguly, A., Y. A. Tang, L. Wang, K. Ladt, J. Loi, B. Dargent, C. Leterrier and Roy, S. h. (2015). A dynamic formin-dependent deep F-actin network in axons. *J. Cell Biol.* **210**, 401-417.
Gaudenz, K., E. Roessler, N. A. Quaderi, B. Franco, G. Feldman, D. L. Gasser, B. Wittwer, E. Montini, J. M. Opitz, A. Ballabio and Muenke, M. (1998). Opitz G/BBB syndrome in Xp22: mutations in the MID1 gene cluster in the carboxy-terminal domain. *Am. J. Hum. Genet.* **63**, 703-710.
Goswami, D., K. Gowrishankar, S. Bilgrami, S. Ghosh, R. Raghupathy, R. Chadda, R. Vishwakarma, M. Rao and Mayor, S. (2008). Nanoclusters of GPI-anchored proteins are formed by cortical actin-driven activity. *Cell* **135**, 1085-1097.
Gowrishankar, K., S. Ghosh, S. Saha, S. Mayor and Rao, M. (2012). Active remodeling of cortical actin regulates spatiotemporal organization of cell surface molecules. *Cell* **149**, 1353-1367.
Hashimoto, Y., S. Maegawa, T. Nagai, E. Yamaha, H. Suzuki, K. Yasuda and Inoue, K. (2004). Localized maternal factors are required for zebrafish germ cell formation. *Dev. Biol.* **268**, 152-161.
Ishihara, K., P. A. Nguyen, A. C. Groen, C. M. Field and Mitchison, T. J. (2014). Microtubule nucleation remote from centrosomes may explain how asters span large cells. *Proc. Natl. Acad. Sci. USA* **111**, 17715-17722.
Jesuthasan, S. (1998). Furrow-associated microtubule arrays are required for the cohesion of zebrafish blastomeres following cytokinesis. *J. Cell Sci.* **111**, 3695-3703.
Juliano, C. E., Swartz, S. Z. and Wessel, G. M. (2010) A conserved germline multipotency program. *Development* **137**, 4113-4126.
Kane, D. A. and Kimmel, C. B. (1993). The zebrafish midblastula transition. *Development* **119**, 447-456.
Knaut, H., F. Pelegri, K. Bohmann, H. Schwarz and Nüsslein-Volhard, C. (2000). Zebrafish *vasa* RNA but not its protein is a component of the germ plasm and segregates asymmetrically prior to germ line specification. *J. Cell Biol.* **149**, 875-888.
Leung, C. F., S. E. Webb and Miller, A. L. (2000). On the mechanism of ooplasmic segregation in single-cell zebrafish embryos. *Dev. Growth Differ.* **42**, 29-40.

Li-Villarreal, N., M. M. Forbes, A. J. Loza, J. Chen, T. Ma, K. Helde, C. B. Moens, J. Shin, A. Sawada, A. E. Hindes, J. Dubrulle, A. F. Schier, G. D. Longmore, F. L. Marlow and Solnica-Krezel, L. (2015). Dachsous1b cadherin regulates actin and microtubule cytoskeleton during early zebrafish embryogenesis. *Development* **142**, 2704-2718.

Miranda-Rodríguez, J. R., E. Salas-Vidal, H. Lomelí, M. Zurita and Schnabel, D. (2017). RhoA/ROCK pathway activity is essential for the correct localization of the germ plasm mRNAs in zebrafish embryos. *Dev. Biol.* **421**, 27-42.

Mohan, R. and John, A. (2016). Microtubule-associated proteins as direct crosslinkers of actin filaments and microtubules. *Int. Union Biochem. Mol. Biol.* **67**: 395-403.

Nair, S., R. E. Lindeman and Pelegri, F. (2013). In vitro oocyte culture-based manipulation of zebrafish maternal genes. *Dev. Dyn.* **242**, 44-52.

Nair, S., F. Marlow, E. Abrams, L. Kapp, M. Mullins and Pelegri, F. (2013). The chromosomal passenger protein Birc5b organizes microfilaments and germ plasm in the zebrafish embryo. *PLoS Genet.* **9**, e1003448.

Nawaz, S., P. Sánchez, S. Schmitt, N. Snaidero, M. Mitkovski, C. Velte, B. R. Brückner, I. Alexopoulos, T. Czopka, S. Y. Jung, J. S. Rhee, A. Janshoff, W. Witke, I. A. T. Schaap, D. A. Lyons and Simons, M. (2015). Actin filament turnover drives leading edge growth during myelin sheath formation in the central nervous system. *Dev. Cell* **34**, 139-151.

Nott, T. J., E. Petsalaki, P. Farber, D. Jervis, E. Fussner, A. Plochowietz, T. D. Craggs, D. P. Bazet-Jones, T. Pawson, J. D. Forman-Kay and Baldwin, A. J. (2015). Phase transition of a disordered nuage protein generates environmentally responsive membraneless organelles. *Mol. Cell* **57**, 936-947.

Olsen, L. C., R. Aasland and Fjose, A. (1997). A vasa-like gene in zebrafish identifies putative primordial germ cells. *Mech. Dev.* **66**, 95-105.

Paksa, A. and Raz, E. (2015). Zebrafish germ cells: motility and guided migration. *Curr. Opin. Cell Biol.* **36**, 80-85.

Pelegri, F., M. P. S. Dekens, S. Schulte-Merker, H.-M. Maischein, C. Weiler and Nüsslein-Volhard, C. (2004). Identification of recessive maternal-effect mutations in the zebrafish using a gynogenesis-based method. *Dev. Dyn.* **231**, 325-336.

Pelegri, F., H. Knaut, H.-M. Maischein, S. Schulte-Merker and Nüsslein-Volhard, C. (1999). A mutation in the zebrafish maternal-effect gene *nebel* affects furrow formation and *vasa* RNA localization. *Curr. Biol.* **9**, 1431-1440.

Pelegri, F. and Schulte-Merker, S. (1999). A gynogenesis-based screen for maternal-effect genes in the zebrafish, *Danio rerio*. In *The Zebrafish: Genetics and Genomics*, Vol. 60 (ed. W. Detrich, L. I. Zon and M. Westerfield), pp. 1-20. San Diego: Academic Press.

Quaderi, N. A., S. Schweiger, K. Gaudenz, B. Franco, E. I. Rugarli, W. Berger, G. Feldman, M. Volta, G. Andolfi, S. Gingenkrantz, R. W. Marion, R. C. M. Hennekam, J. M. Opitz, M. Muenke, H. H. Ropers and Ballabio, A. (1997). Opitz G/BBB syndrom, a defect of midline development, is due to mutations in a new RING finger gene on Xp22. *Nat. Genet.* **17**, 285 - 291.

Ressom, R. E. and Dixon, K. E. (1988) Relocation and reorganization of germ plasm in Xenopus embryos after fertilization. *Development* **103**, 507-518.

Riemer, S., F. Bontems, P. Krishnakumar, J. Gomann and Dosch, R. (2015). A functional Bucky ball-GFP transgene visualizes germ plasm in living zebrafish. *Gene Exp. Patterns* **18**, 44-52.

Roosen-Runge, E. C. (1938). On the early development-bipolar differentiation and cleavage of the zebra fish, *Brachydanio rerio*. *Biol. Bull.* **75**, 119-133.
Saha, S., I.-H. Lee, A. Polley, J. T. Groves, M. Rao and Mayor, S. (2015). Diffusion of GPI-anchored proteins is influenced by the activity of dynamic cortical actin. *Mol. Biol. Cell* **26**, 4033-4045.
Savage, R. and Danilchik, M. V. (1993). Dynamics of germ plasm localization and its inhibition by ultraviolet irradiation in early cleavage *Xenopus* embryos. *Dev. Biol.* **157**, 371-382.
Schaefer, A. W., N. Kabir and Forscher, P. (2002). Filopodia and actin arcs guide the assembly and transport of two populations of microtubules with unique dynamic parameters in neuronal growth cones. *J. Cell Biol.* **158**, 139-152.
Strome, S. and Lehmann, R. (2007). Germ versus soma decisions: lessons from flies and worms. *Science* **316**, 392-393.
Theusch, E. V., K. J. Brown and Pelegri, F. (2006). Separate pathways of RNA recruitment lead to the compartmentalization of the zebrafish germ plasm. *Dev. Biol.* **292**, 129-141.
Updike, D. L., S. J. Hachey, J. Kreher and Strome, S. (2011). P granules extend the nuclear pore complex environment in the *C. elegans* germ line. *J. Cell Biol.* **192**, 939-948.
Urven, L. E., T. Yabe and Pelegri, F. (2006). A role for non-muscle myosin II function in furrow maturation in the early zebrafish embryo. *J. Cell Sci.* **119**, 4342-4352.
Wang, J. T., J. A. Smith, B. C. Chen, H. Schmidt, D. Rasoloson, A. Paix, B. G. Lambrus, D. Calidas, E. Betzig and Seydoux, G. (2014). Regulation of RNA granule dynamics by phosphorylation of serine-rich, intrinsically disordered proteins in *C. elegans*. *eLife* **3**, e04591.
Weidinger, G., J. Stebler, K. Slanchev, K. Dumstrei, C. Wise, R. Lovell-Badge, C. Thisse, B. Thisse and Raz, E. (2003). *dead end*, a novel vertebrate germ plasm component, is required for zebrafish primordial germ cell migration and survival. *Curr. Biol.* **13**, 1429-1434.
Whittington, P. M. and Dixon, K. E. (1975) Quantitative studies of germ plasm and germ cells during early embryogenesis of Xenopus laevis. *J Embryol Exp Morph* **33**, 57-74.
Winter, J., T. Lehmann, V. Suckow, Z. Kijas, A. Kulozik, V. Karlsheuer, B. Hamel, K. Devriendt, J. M. Opitz, S. Lenzner, H.-H. Ropers and Schweiger, S. (2003). Duplication of the *MID1* first exon in a patient with Opitz G/BBB syndrome. *Hum. Genet.* **112**, 249-254.
Wühr, M., S. Dumont, A. C. Groen, D. J. Needleman and Mitchison, T. J. (2009). How does a millimeter-sized cell find its center? *Cell Cycle* **8**, 1115-1121.
Wühr, M., E. S. Tan, S. K. Parker, H. W. I. Detrich and Mitchinson, T. J. (2010). A model for cleavage plane determination in early amphibian and fish embryos. *Curr. Biol.* **20**, 2040-2045.
Wylie, C. (1999). Germ cells. *Cell* **96**, 165-174.
Yabe, T., X. Ge, R. Lindeman, S. Nair, G. Runke, M. Mullins and Pelegri, F. (2009). The maternal-effect gene *cellular island* encodes Aurora B kinase and is essential for furrow formation in the early zebrafish embryo. *PLoS Genet.* **5**, e1000518.
Yoon, C., K. Kawakami and Hopkins, N. (1997). Zebrafish *vasa* homologue RNA is localized to the cleavage planes of 2- and 4-cell-stage embryos and is expressed in the primordial germ cells. *Development* **124**, 3157-3165.
Zuchero, J. B., M.-m. Fu, S. A. Sloan, A. Ibrahim, A. Olson, A. Zaremba, J. C. Dugas, S. Wienbar, A. V. Caprariello, C. Kantor, D. Leonoudakis, K. Lariosa-Willingham, G. Kronenberg, K. Gertz, S. H. Soderling, R. H. Miller and Barres, B. A. (2015). CNS myelin wrapping is driven by actin disassembly. *Dev. Cell* **34**, 152-167.

Figures

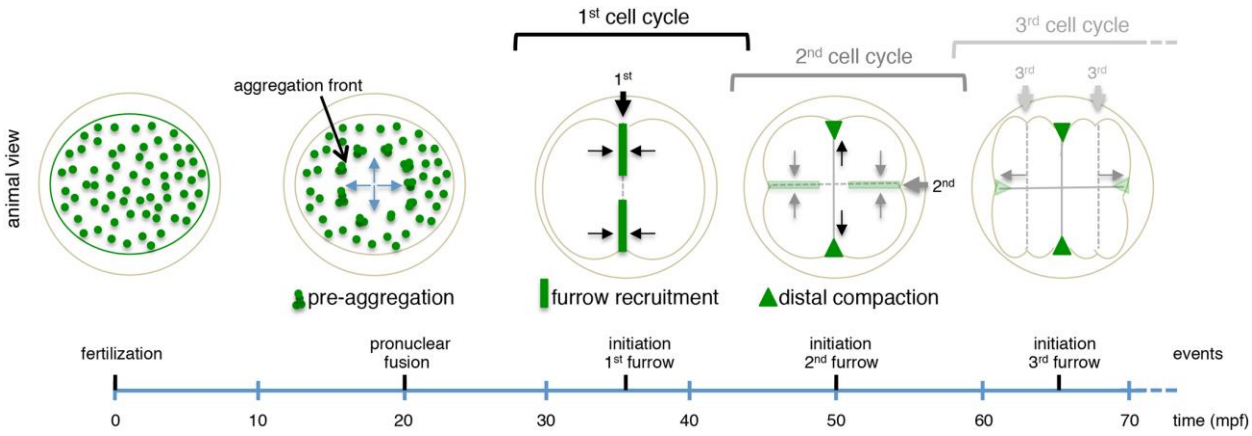

Figure 1: Stages of RNP segregation leading to germ plasm aggregates at the furrow. Radial astral microtubule growth results in the outward movement of RNPs, which begin a process of pre-aggregation even prior to furrow formation. During cell division, the same process but now driven by microtubules from a bipolar spindle (not shown) result in the RNP recruitment at the furrow. Medial-to-distal movement along the furrow generates compact masses at the furrow distal ends. The process is systematically repeated through the early cell divisions, although only the largest four germ plasm masses, corresponding to those at the first and second cleavage furrows, are stable (Eno and Pelegri, 2013; Eno and Pelegri, 2016).

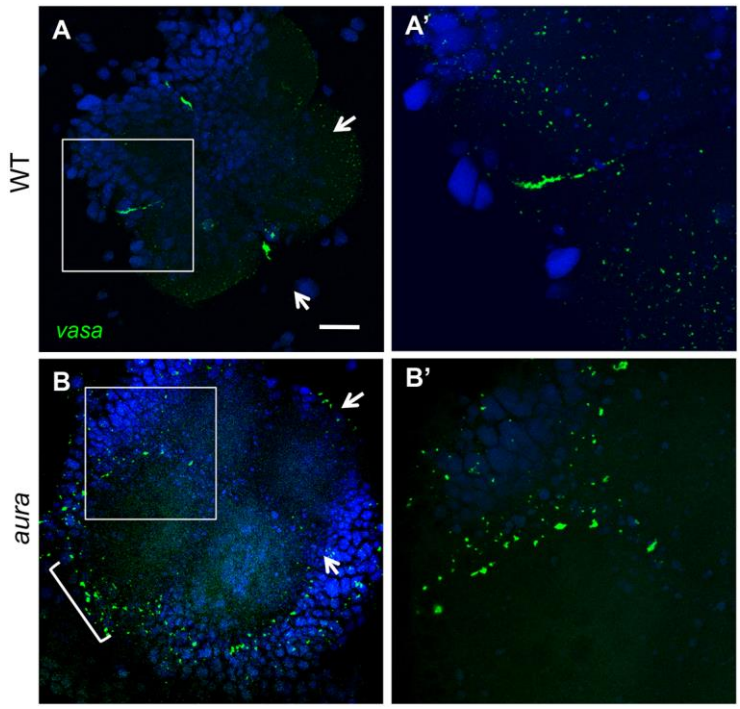

Figure 2: *aura* mutant embryos fail to recruit germ plasm to the furrows. (A.B) *vasa* RNA localizes to the furrow in wild-type (A,A') but not in *aura* mutants (B,B'), where it instead localizes to the blastodisc periphery (B, bracket). Arrows indicate cleavage planes for the first and second cell cycles. Scale bars: 100 μM (A,B), 10 μM (A',B').

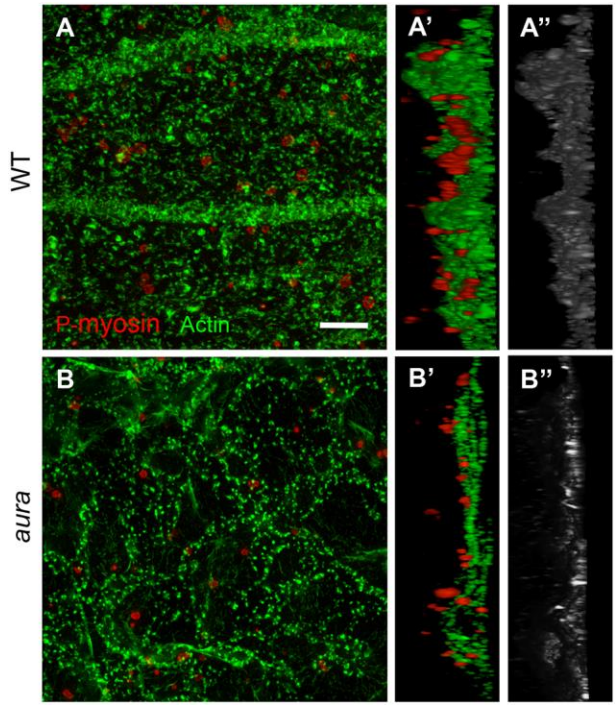

Figure 3: Germ plasm RNP aggregates associate with Mid1ip1L-dependent cortical F-actin contractions. (A,B) SIM images of cortical F-actin and germ plasm RNPs (anti-P-myosin) in wild-type (A) and *aura* mutants (B), with orthogonal views (A',B': F-actin/RNPs; A",B": F-actin alone). Scale bar: 5 μM (C-D').

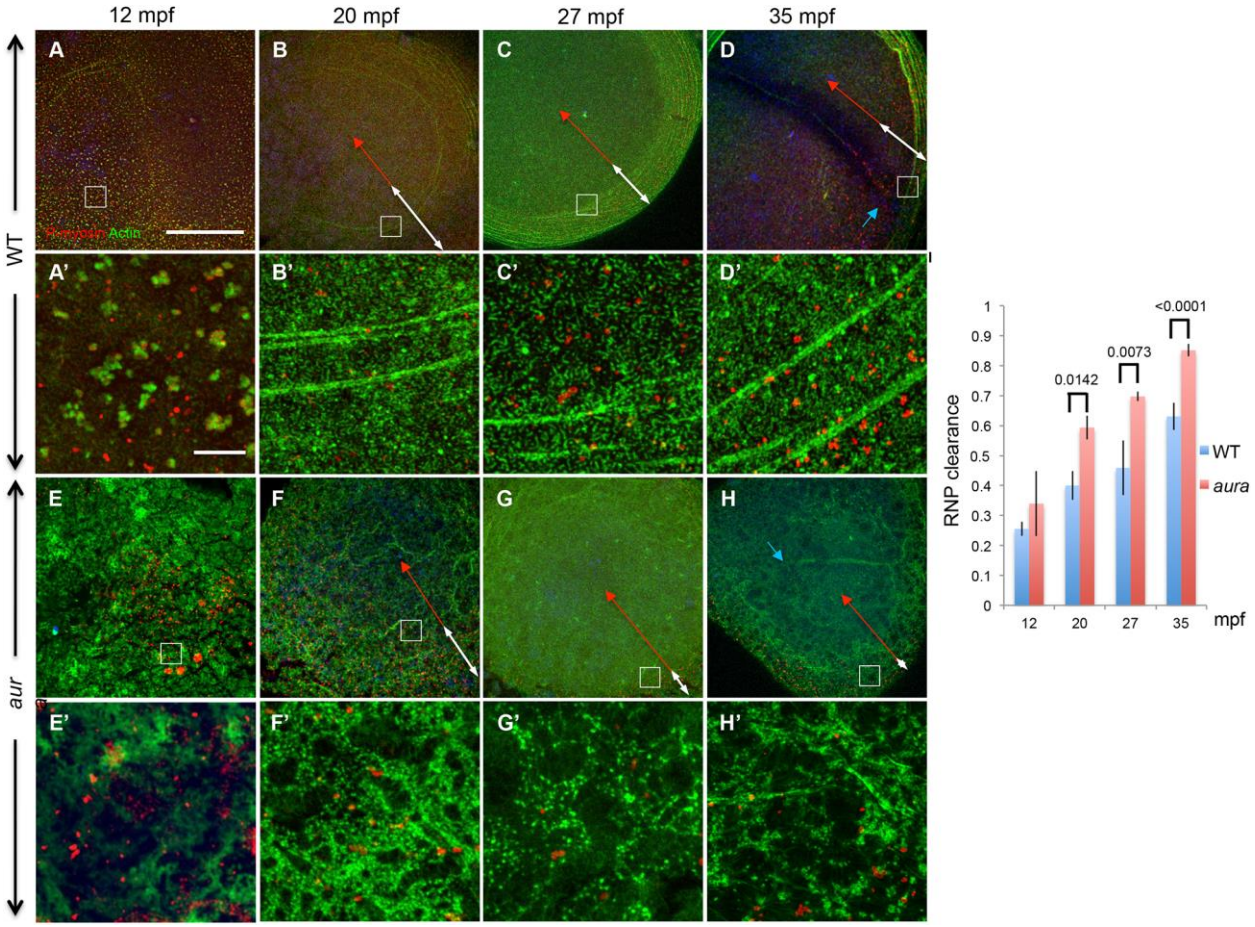

Figure 4: Increased outward movement of germ plasm RNPs in *aura/mid1ip1L* mutants. (A-D) In wild-type embryos, RNPs, initially distributed throughout the blastodisc, progressively accumulate as a peripheral band coincident with F-actin arc formation and peripheral movement. (E-H) In *aura* mutants, F-actin arcs fail to form and the field of RNPs narrows at a faster rate. White double arrows highlight the RNP field, and red double-arrows indicate the distance from the center of the embryo to the inner rim of aggregates at the RNP field. Blue arrows (D,H) indicate furrow F-actin. A'-H' are magnified regions of A-H at the location indicated by inserts. Scale: 100 μM A-H (bar in A), 10 μM A'-H' (bar in A'). (I) Quantitation of outward RNP movement, with the location of the RNP aggregating front determined upon magnification of the image. Significance using unpaired T-test.

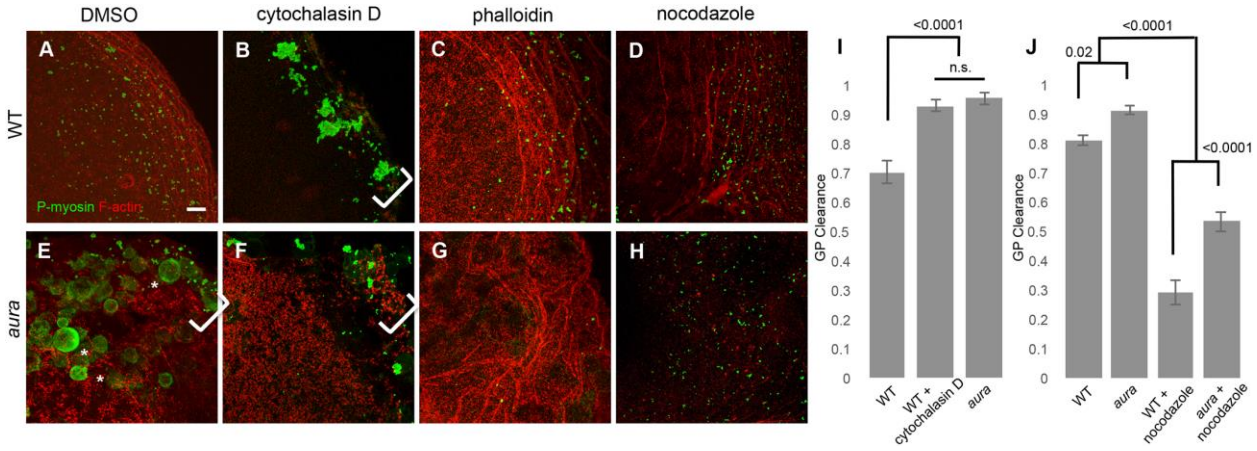

Figure 5: Modulation of germ plasm RNP outward movement depends on cortical F-actin. RNPs (green) and cortical F-actin (red) in control- (DMSO), cytochalasin D-, phalloidin-, and nocodazole-treated wild-type (A-D) and *aura* mutant (E-H) embryos. F-actin inhibition with cytochalasin D in wild-type embryos leads to large RNP aggregates at the distal edge of the blastodisc (B), mimicking the *aura* mutant phenotype (E; large spherical structures are retained cortical granules; Eno et al., 2016). F-actin stabilization with phalloidin (C) does not have a significant effect in wild-type (A') but reduces ectopic RNP aggregate accumulation in *aura* mutants (G). Inhibition of microtubules with nocodazole results in reduced outward RNP movement in both wild type (D; Theusch et al., 2006), and *aura* mutants (H). Brackets indicate ectopic marginal RNP aggregate accumulation. (I,J) Quantitation of RNP outward clearing as in Fig. 4. Scale: 10 μM (bar in A).

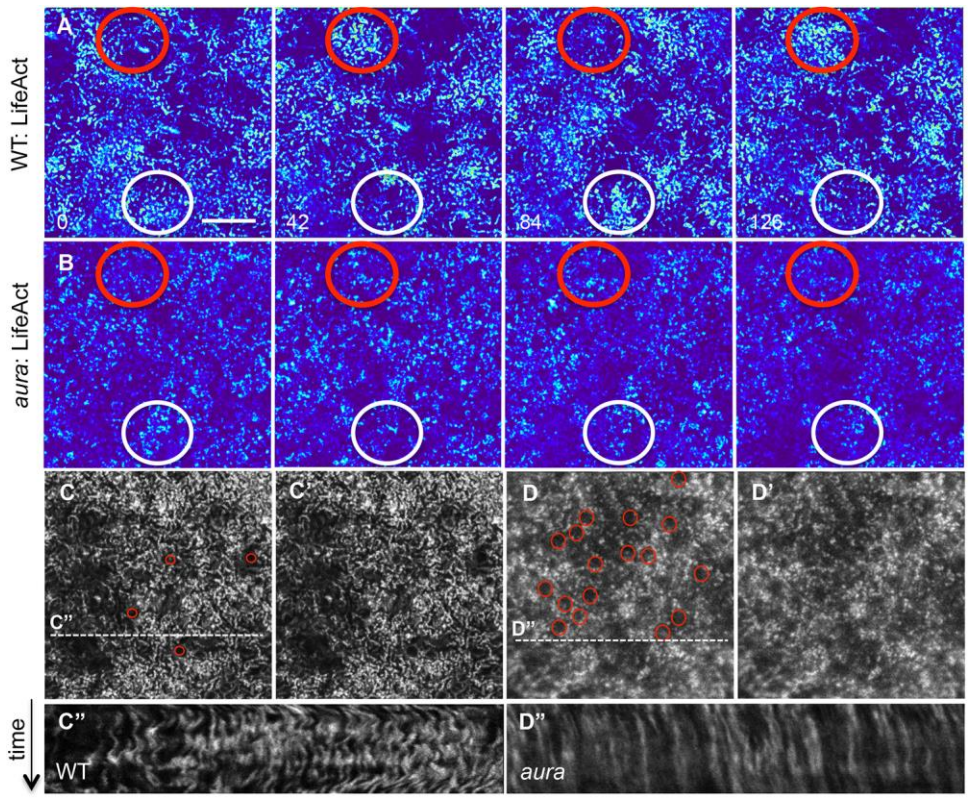

Figure 6: Dynamic waves of cortical F-actin depend on *aura/mid1ip1* function. (A,B) In live wild-type embryos, cortical F-actin shows cyclical patterns of apparent enrichment, whereas this network appears static in *aura* mutants (B) (in each case, red and white circles highlight two different cortical locations). Still images of LifeAct transgenic embryos spaced 42 sec apart (Movies 1 and 2). (C,D) Still images of F-actin network towards the end of the movie sequence highlighting that F-actin forms a punctate pattern as well as numerous round F-actin structures (red circles) in mutants (D,D') present in lower numbers in wild-type (D,D'). (C",D") Kymographs of cortical F-actin (data from dashed line in C',D', representing 70 time points in a 140 sec period) shows lateral undulations in wild type and a static network in *aura* mutants. Scale: 10 μM A-C (bar in A).

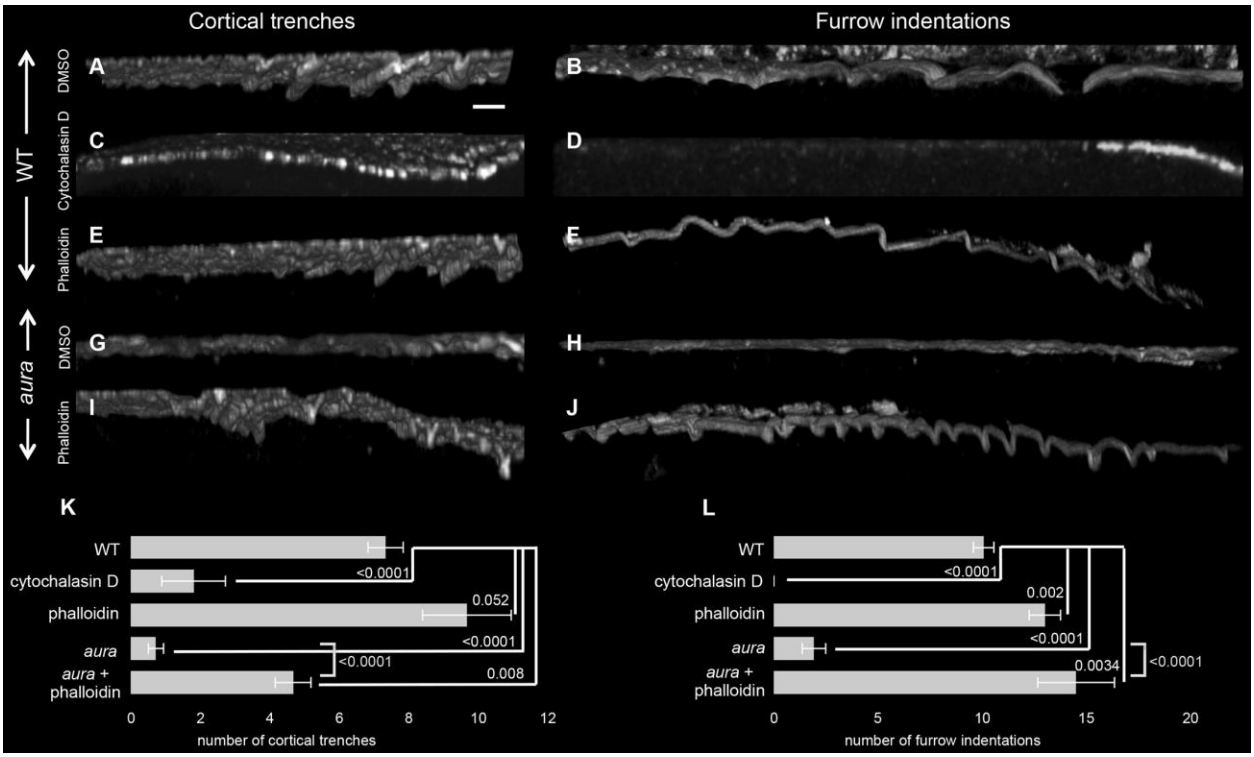

Figure 7: F-actin cortical trenches and furrow indentations depend on *aura/mi1ip1L* function. Orthogonal views of cortical and furrow F-actin in wild-type and *aura* mutant embryos treated with drugs targeting F-actin. Wild-type embryos exhibit cortical trenches (A) and furrow indentations (B), which are missing in *aura* mutants (G,H). In wild-type, actin inhibition with cytochalasin D abolishes the formation of both cortical trenches (C) and furrow indentations (D). Treatment with the F-actin stabilizer phalloidin allows cortex trenches (E) and furrow indentations (F) in wild-type and rescues the formation of these structures in *aura* mutants (I,J). (K,L) Quantitation of the number of cortical trenches and furrow indentations under the various conditions, using data from at least 7 images per condition.

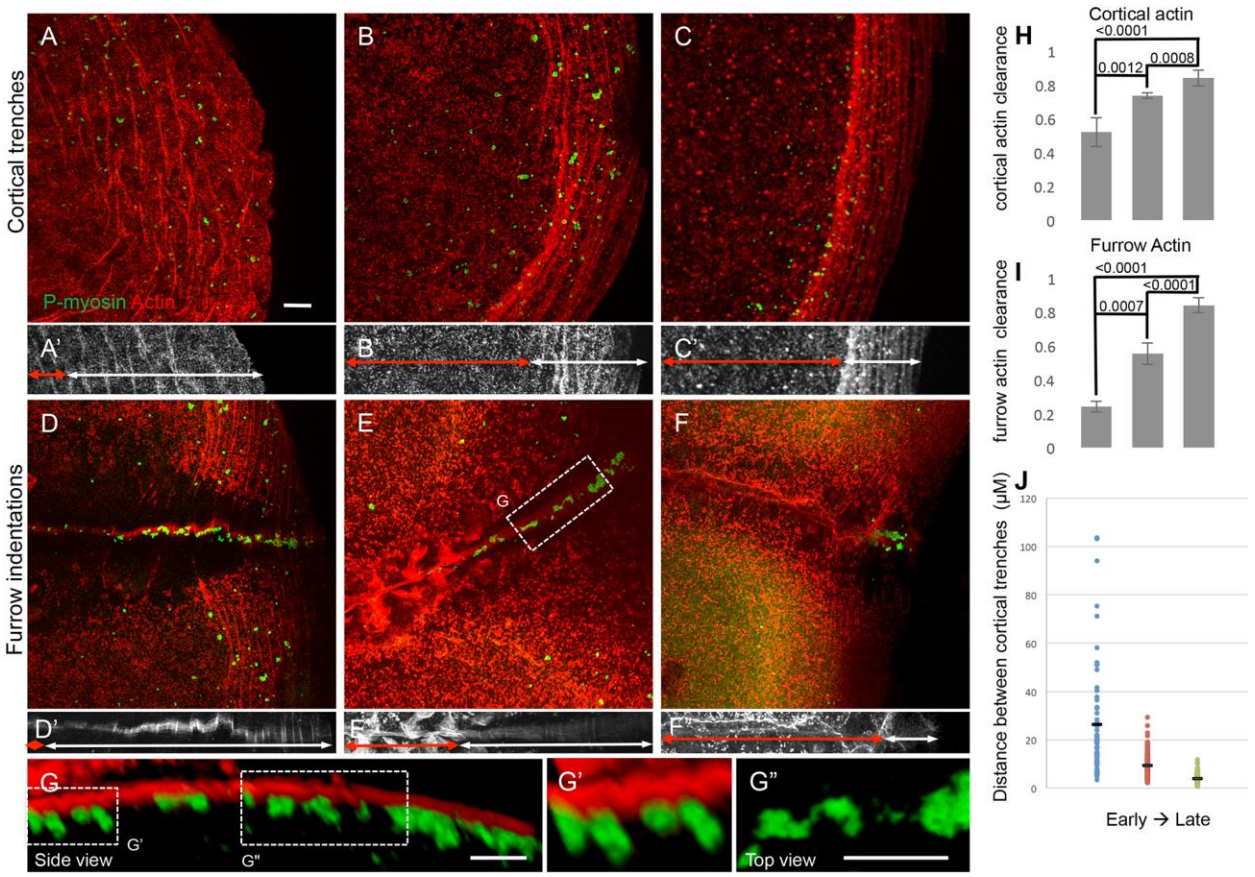

Figure 8: F-actin cortical trenches and furrow indentations exhibit a directional progression and are associated with germ plasm RNPs. (A-C) Wild-type embryos fixed prior to furrow formation (A: 35 mpf, B: 50 mpf, C: 65 mpf, animal with blastodisc center to the left and blastodisc periphery to the right). F-actin arcs, associated with RNP aggregates, move outwards as they form a more dense network. Inserts in (A'-C') highlight the region of F-actin arcs (white double arrows) and the distance from the center of the blastodisc to the inner rim of the F-actin arc region (red double arrows). (D-F) Wild-type embryos fixed during furrow formation (D: 35 mpf, E: 50 mpf, F: 65 mpf, animal view with furrow medial region to the left and furrow distal end to the right). The region containing RNPs, which progressively becomes more distally restricted, corresponds to that exhibiting F-actin furrow indentations as revealed by orthogonal views (D'-F'). In (D'-F'), white double arrows encompass the region with F-actin indentations and red double arrows the more medial region with F-actin of an even and wider span and with a punctate appearance, which likely correspond to the forming cell adhesive wall (Jesuthasan, 1998; Urven et al., 2006). (G) Orthogonal view of the furrow showing association of RNP aggregates with F-actin furrow indentations. (G') Insert showing RNP aggregates wedged within cytoplasmic spaces between indentations. (G") Insert (rotated as a top view for better visualization) shows an apparent stream of individual RNPs between larger aggregates. In all

images RNPs (P-myosin) are in green and F-actin in red, except the F-actin channel has been omitted for clarity in (A-C',D'-F' and G"). (H) Quantification of cortical actin clearance as the ratio of the distance from the center of the blastodisc to the region of cortical F-actin trenches (red double arrows in A'-C') over the blastodisc radius. (I) Quantification of furrow actin clearance as the distance from the center of the furrow to the region of furrow F-actin indentations (red double arrows in D'-F') over the half-length of the furrow. (J) Quantification of the distance between individual F-actin arcs (distance between their peak intensity) within the blastodisc arc region (double arrows in A'-C'), showing increasing density of F-actin network during its peripheral restriction. Scale: 10 μM A-F (bar in A, G, G')

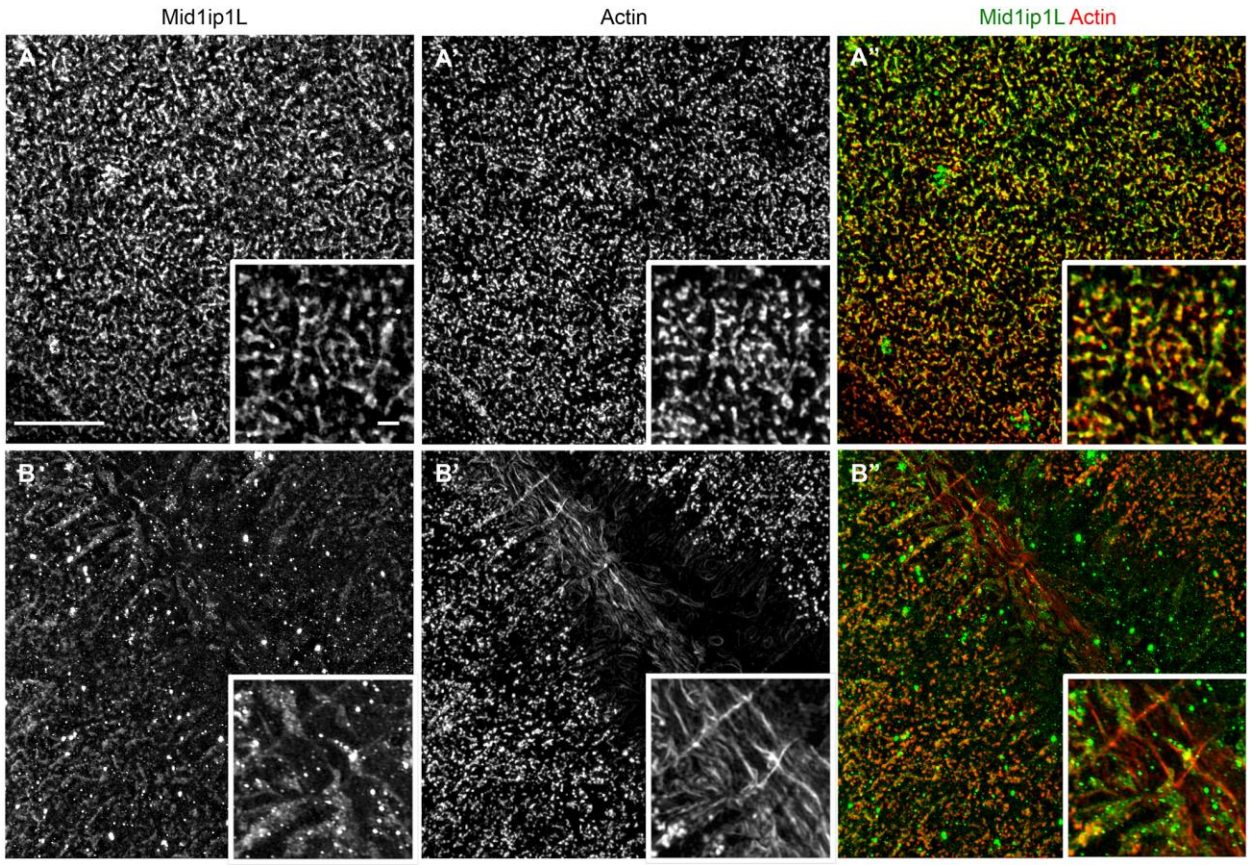

Figure 9: Mid1ip1L protein localizes with cortex and furrow actin. (A,B) SIM images of single and merged channels showing partial colocalization of Mid1ip1L protein with F-actin in wild-type embryos. (A) At the cortex, Mid1ip1L protein partially colocalizes with the cortical F-actin. (B) At the furrow, Mid1ip1L protein also partially colocalizes with traverse F-actin at furrow distal ends, which corresponds to furrow F-actin indentations (see also Fig. S5). Inserts show a magnified view within the field. Scale: 10 μM A-B" (bar in A), 1 μM insets (bar in A inset).

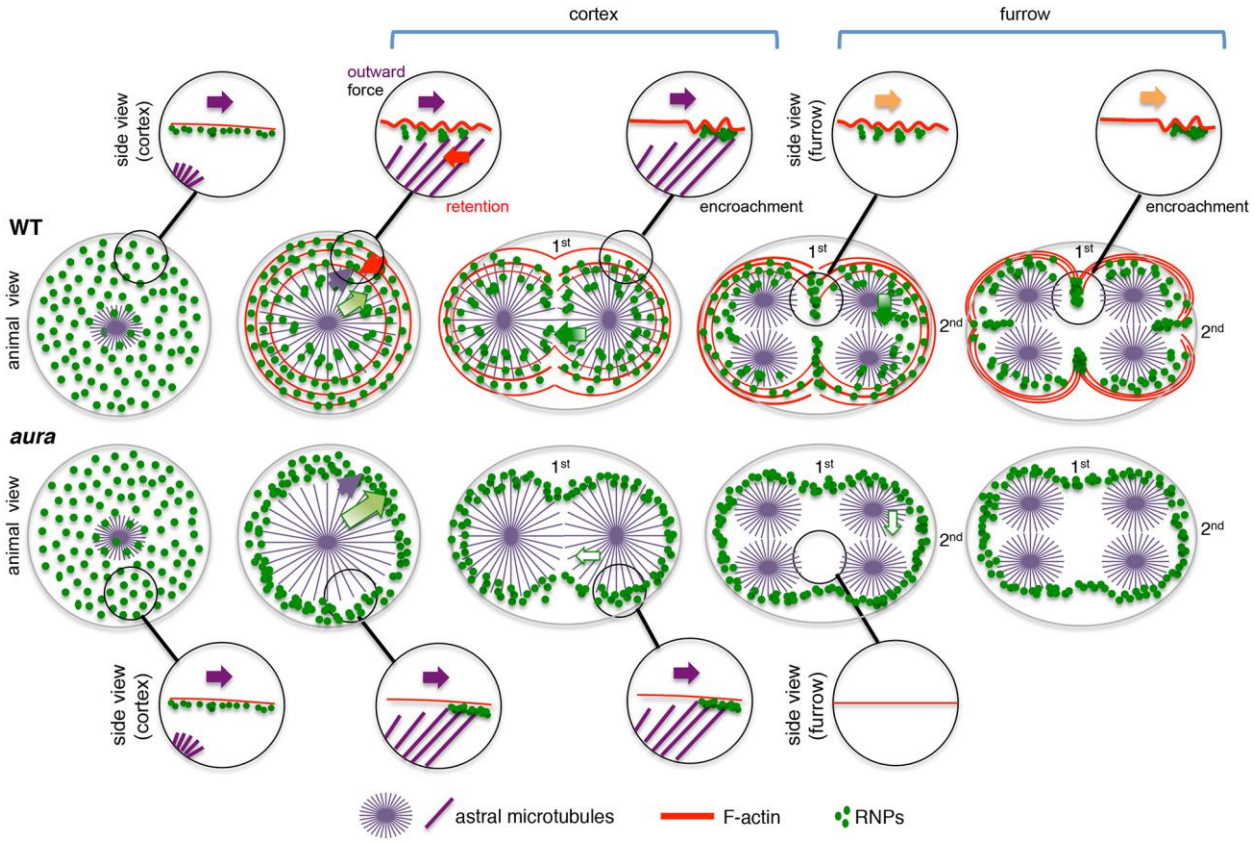

Figure 10: Model for the Mid1ip1L- and F-actin-dependent modulation of germ plasm segregation. In wild-type (WT, animal view) during the first several cell cycles, Mid1ip1L-dependent F-actin dynamics attenuates (red arrows) a microtubule-dependent outward movement (purple arrows) resulting in the regulated outward movement of RNPs (graded light green arrow). Regulated outward RNP movement allows the partial persistence of RNPs at the cortex, making them available for recruitment to the furrows for the next cell cycles (graded dark green arrow). In *aura* mutants (animal view), Mid1ip1L-dependent modulation is affected, causing unregulated outward RNP movement. This results in low persistence of RNPs at the cortex, leading to reduced RNP furrow recruitment (hollow green arrow) and increased peripheral accumulation. Insets as side views depict shared aspects of Mid1ip1L-dependent surface contractions at the cortex and along the furrow, whose gradual increase in density facilitates RNP aggregate fusion through encroachment. Growing astral microtubules likely provide a directional outward radial cue to influence cortical contractions. A second signal (yellow arrows) provides medial-to-distal directionality along the furrow (see accompanying Eno et al manuscript; furrow associated microtubules are not shown).

Supplementary Data

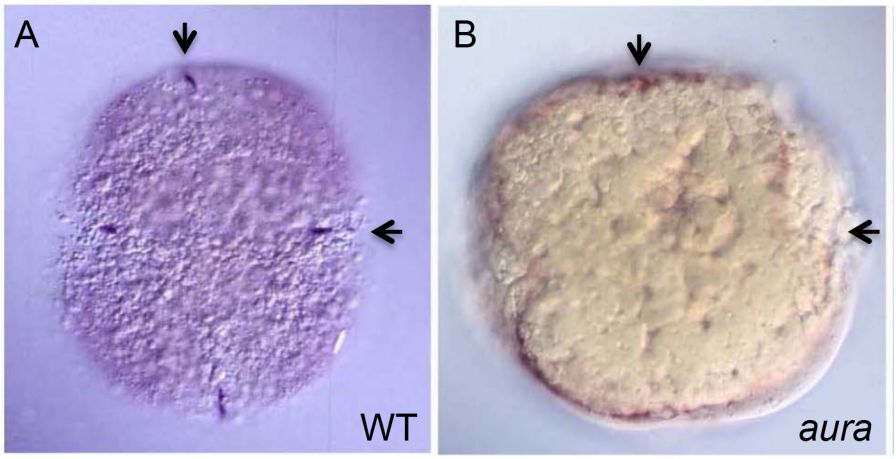

Figure S1: *vasa* RNA localization in *aura* mutant embryos. 4-cell stage embryos showing normal RNA furrow localization in wild-type (A) and reduced furrow localization and increase marginal enrichment in *aura* mutants (B). *vasa* RNA visualized as in Fig. 2A,B but using DAB (blue) visible substrate. Arrows show cleavage planes.

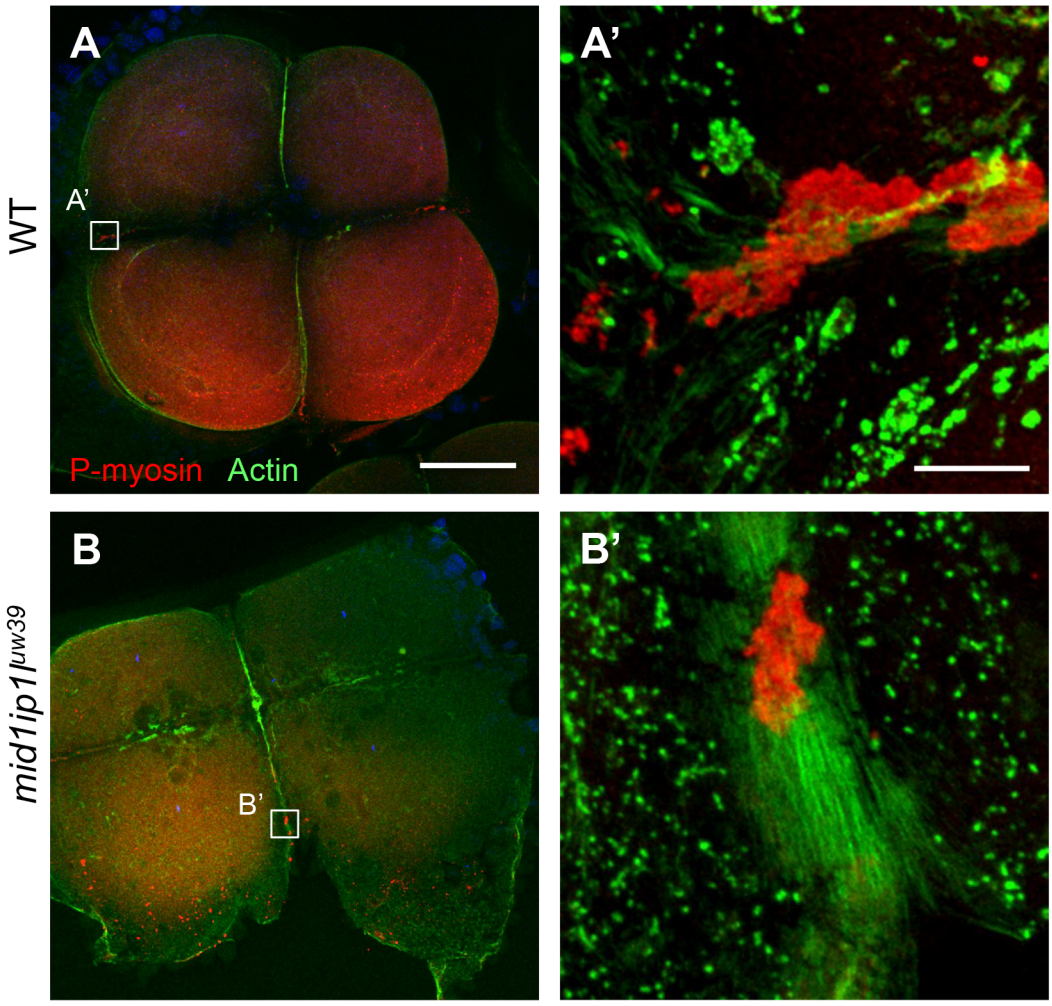

Figure S2: Maternal-effect germ plasm segregation defect in mutants for *mid1ip1l*^{uw39}. Localization of RNPs (using an anti-P-myosin antibody) and F-actin in wild-type (A, A') and embryos from females homozygous for the *mid1ip1l*^{uw39} alllele (B,B'). Scale: 100 µM A-D (bar in A), 10 µM A',B' (bar in A').

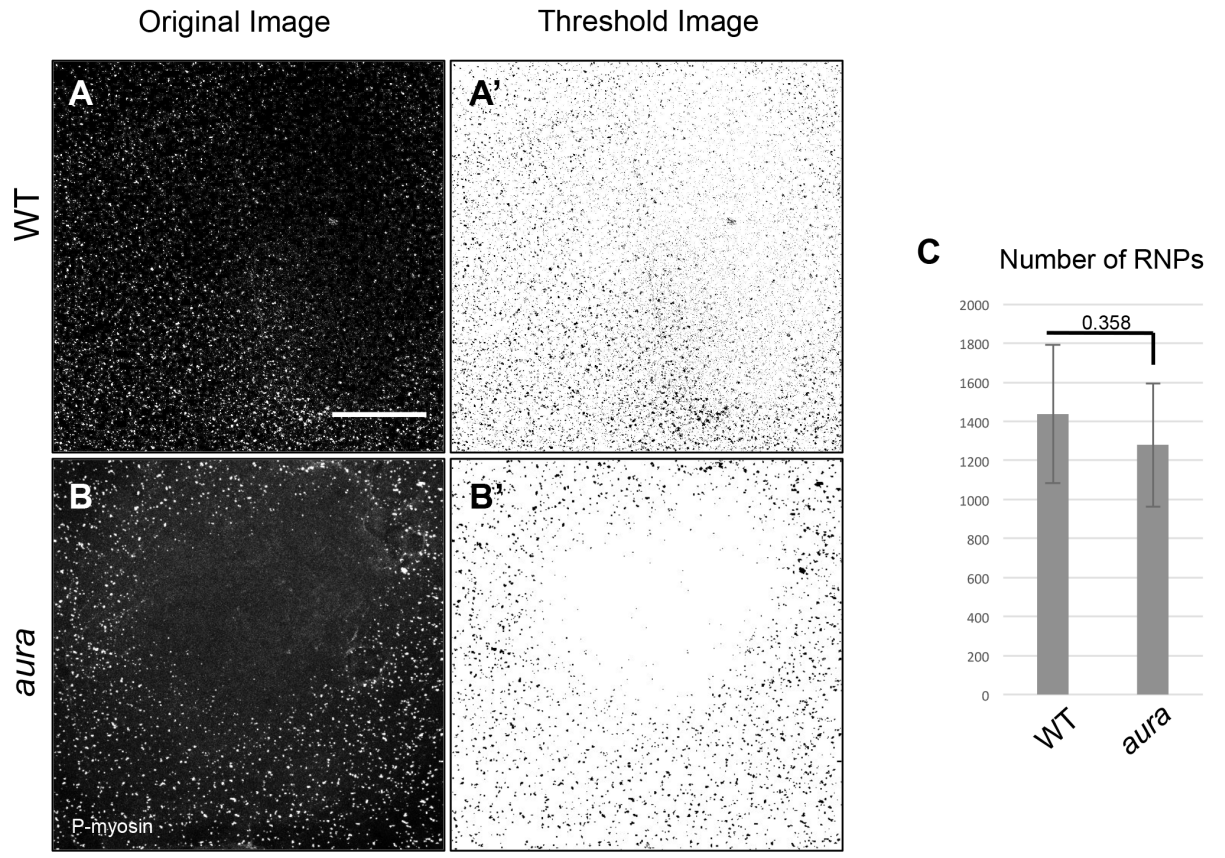

Figure S3: *aura* mutant embryos exhibit a similar initial number of cortical germ plasm RNPs. Wild-type and *aura* mutant embryos fixed at 12 mpf show a similar number of RNPs. (A.B) Labeling of RNP with anti-P-myosin. (A',B') Reversed grayscale for improved visualization. The RNP zone in the center of the blastodisc is likely the incipient zone of RNP clearing, which our observations suggest moves outward faster in *aura* mutants than in wild-type. (C) Quantification of the number of spots in image fields using automated particle counting (FIJI) shows no statistically significant difference between wild-type and mutant embryos (8 embryos each). Scale: 100 μM.

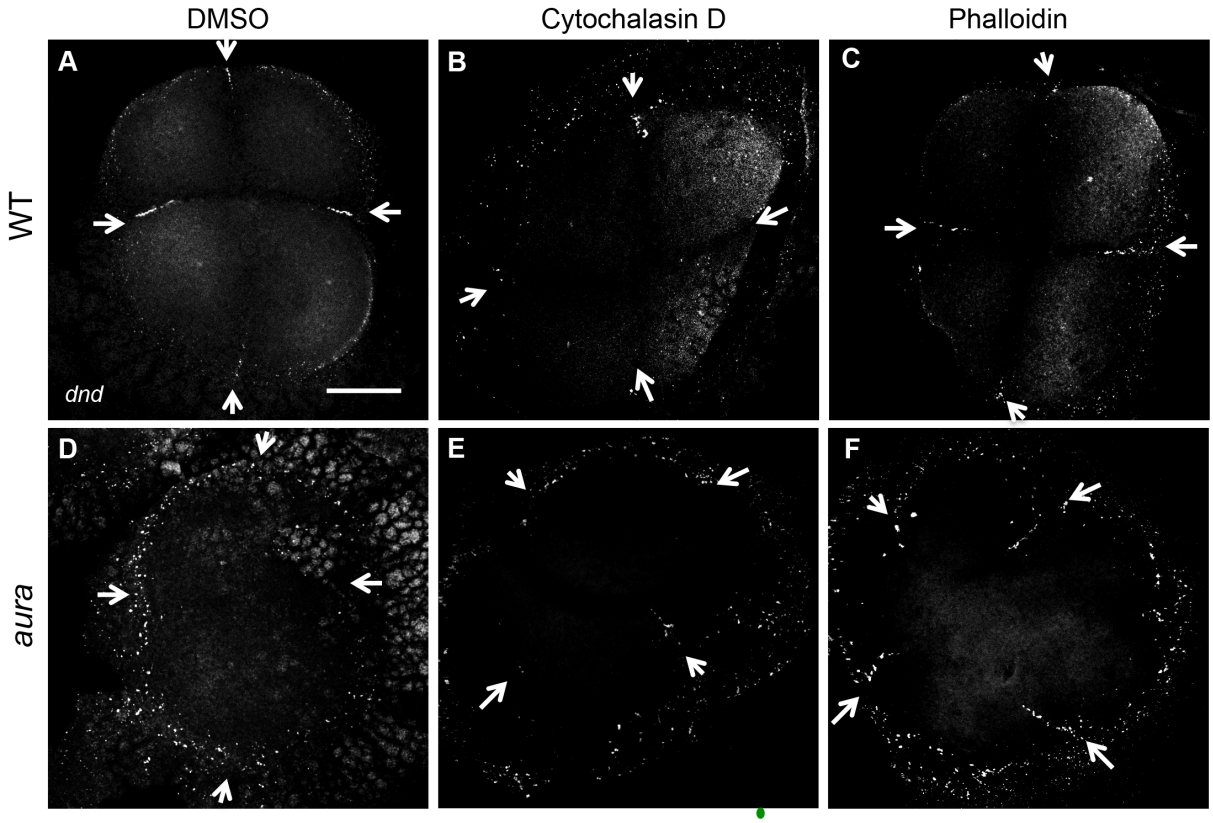

Figure S4: Effects of cytoskeletal inhibitors on germ plasm RNP furrow recruitment.
Fluorescent in situ hybridization to visualize *dnd* RNA localization. Scale: 100 µM A-F (bar in A)

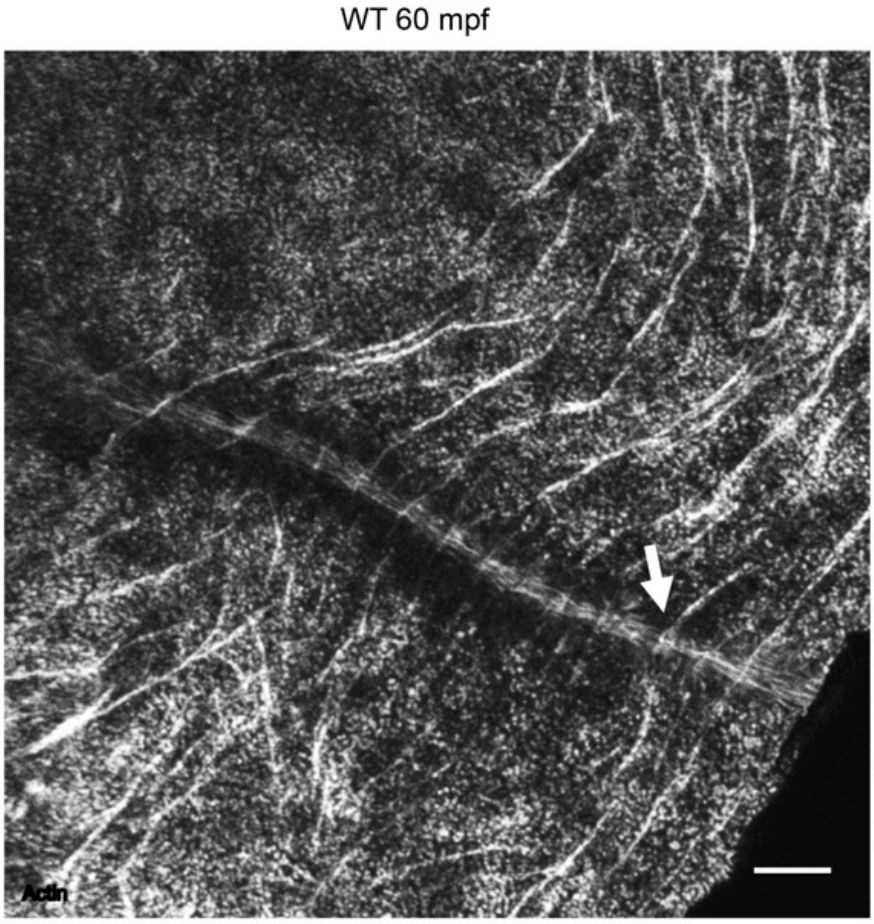

Figure S5: F-actin cortical trenches converge with F-actin furrow indentations. Overview of a wild-type embryo labeled for F-actin, showing that many circumferential F-actin arcs, which correspond to cortical trenches (Fig. 7A), connect to F-actin enrichments at the furrow (Fig. 7B), which correspond to furrow indentations.

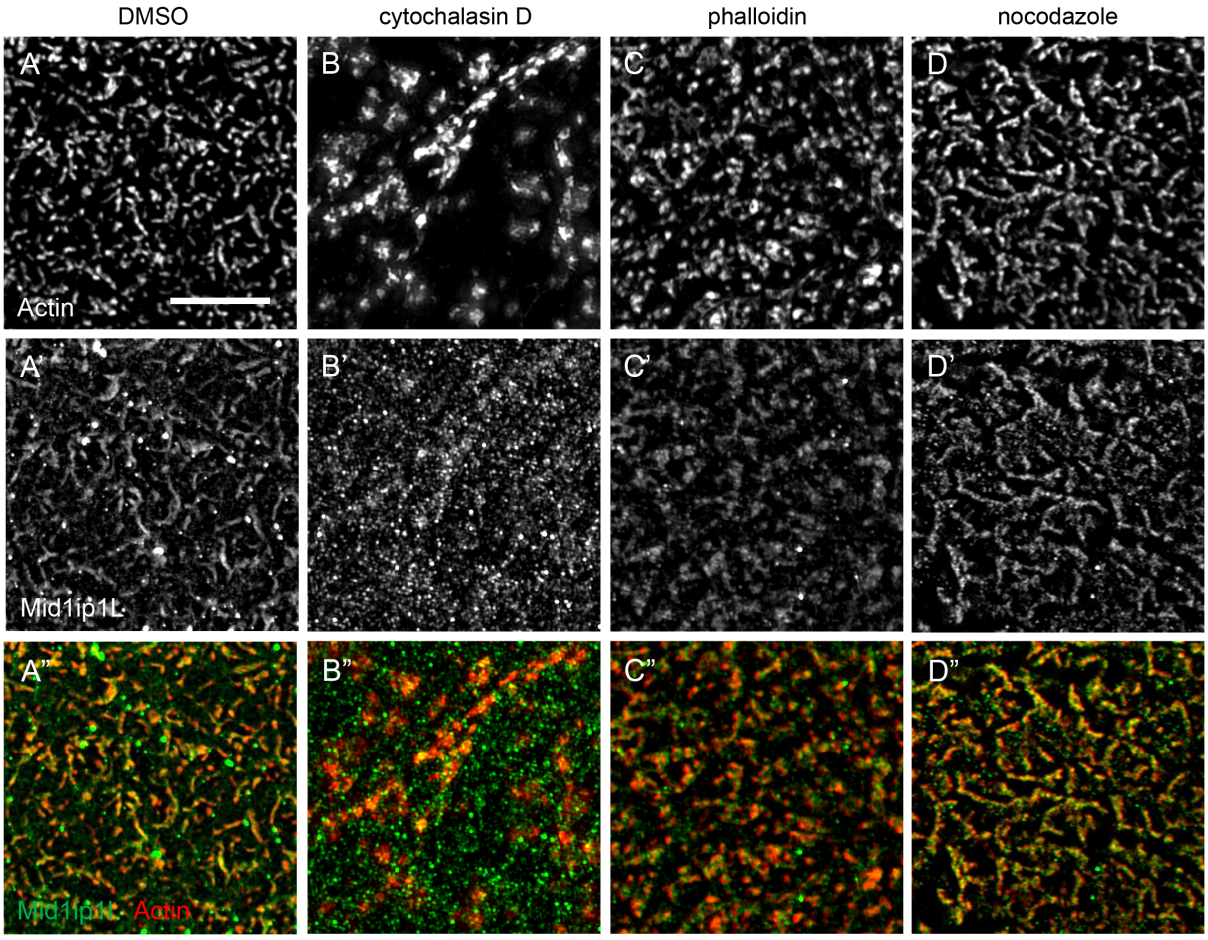

Figure S6: Mid1ip1L protein localization depends on F-actin, but not microtubules. SIM images showing localization of Mid1ip1l with respect to F-actin in the presence of cytoskeletal inhibitors. Both actin inhibition (B-B") and stabilization (C-C") lead to a reduction in colocalization. Colocalization appears unaffected by microtubule inhibition (D-D"). Scale: 5 μM A-H (bar in A).

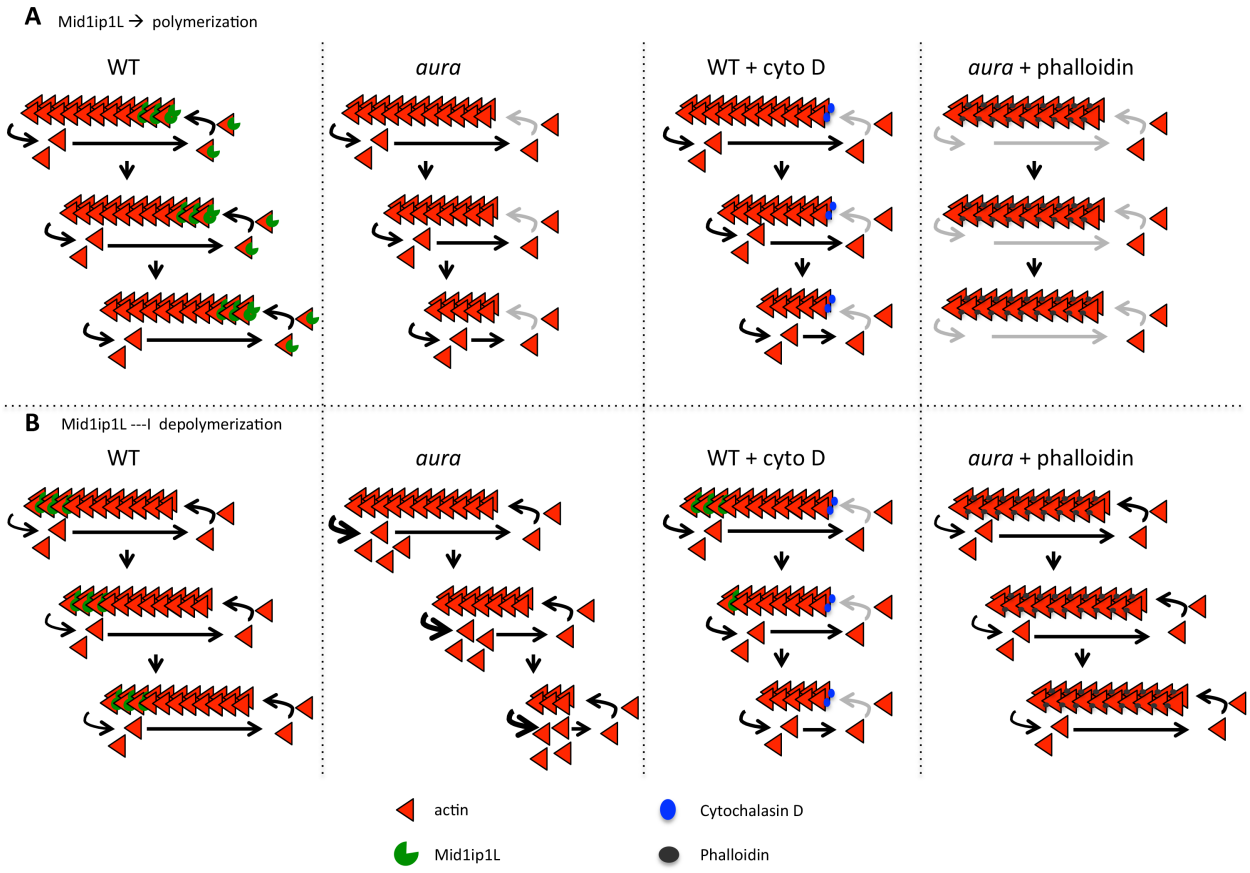

Figure S7: Potential mechanisms by which Mid1ip1L may regulate actin dynamics, and relation to inhibitor effects. Models based on the observed binding of Mid1ip1L to one end of short F-actin (Fig. 9), and effects of the cytochalasin D and phalloidin on the *aura* phenotype. A) Mid1ip1L promotes F-actin polymerization at the site of actin monomer addition (plus ends), so that reduced function results in decreased polymerization. B) Mid1ip1L downregulates the rate of F-actin depolymerization at the minus ends, so that the reduced function results in increased F-actin depolymerization. In both models, both *aura* mutants and cytochalasin D-treated wild-type embryos exhibit F-actin loss. In both models, stabilization of F-actin with phalloidin reduces the rate F-actin loss, allowing for the formation of short F-actin and partially rescuing the phenotype. Plus (barbed) end are shown on right and minus (pointed) ends on left, with F-actin treadmilling indicated by growth to the right from top (early in sequence) to bottom (later in sequence).

Table S1. Primers used for end-point genotyping.

Primer Name	5'-> 3'	Use
mid1ip1L Forward	TATCACCTCCACGGACTCTT	genotyping
mid1ip1L Reverse	CCGCCGATTTCTCTCTTGT	genotyping
mid1ip1L MUT Probe	/56FAM/TGT +C+C+T +AA+C +TAA C/3IABkFQ/	genotyping
mid1ipL WT Probe	/5HEX/TGT +C+C+A +AA+C T+AA CA/3IABkFQ/	genotyping

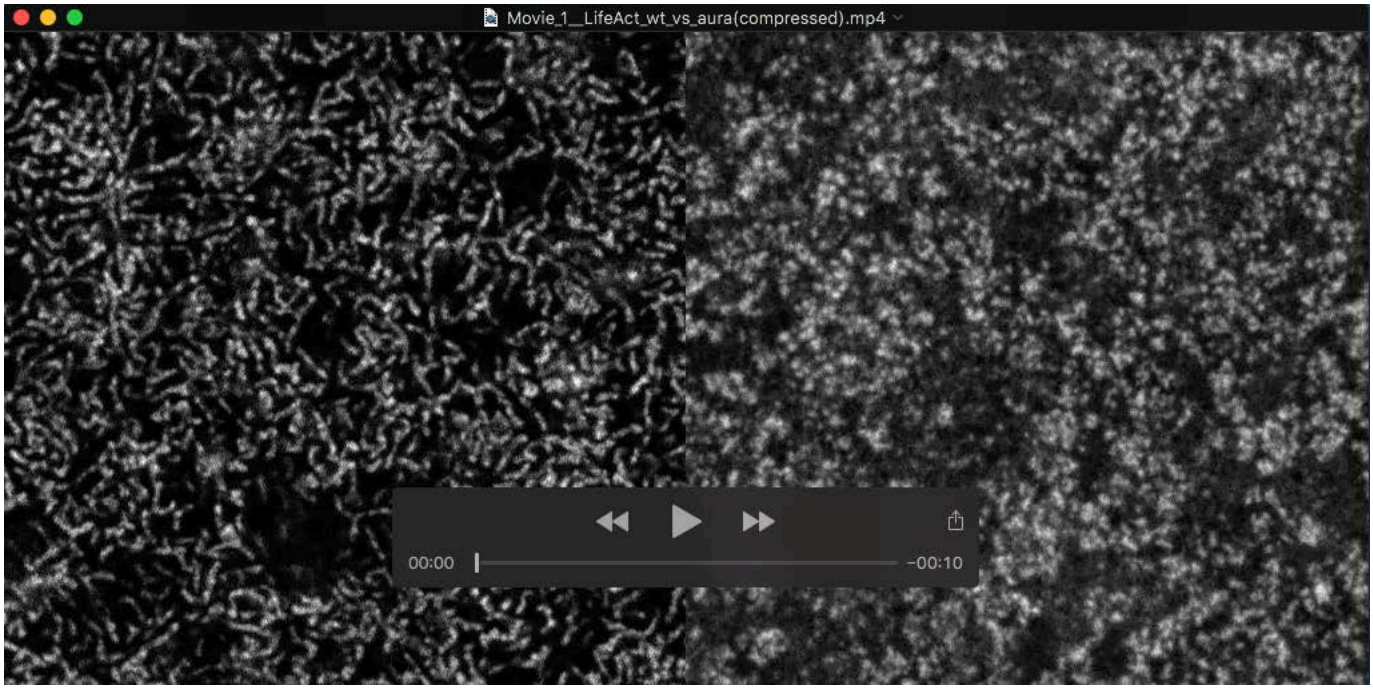

Movie 1. Cortical F-actin in live embryos: wild-type vs *aura* mutants. Left: In wild-type, cortical F-actin exhibits dynamic cyclical changes and local undulations. Movie corresponds to still data in Fig. 6A. Representative movie of 10 trials. Right: In *aura* mutants, cortical F-actin appears static and exhibits an aberrant reorganization. Movie corresponds to still data in Fig. 6B. Representative movie of 10 trials. In both movies, F-actin is detected by the Life Act transgene, with images at 200x magnification, corresponding to scale bar in Fig. 6.

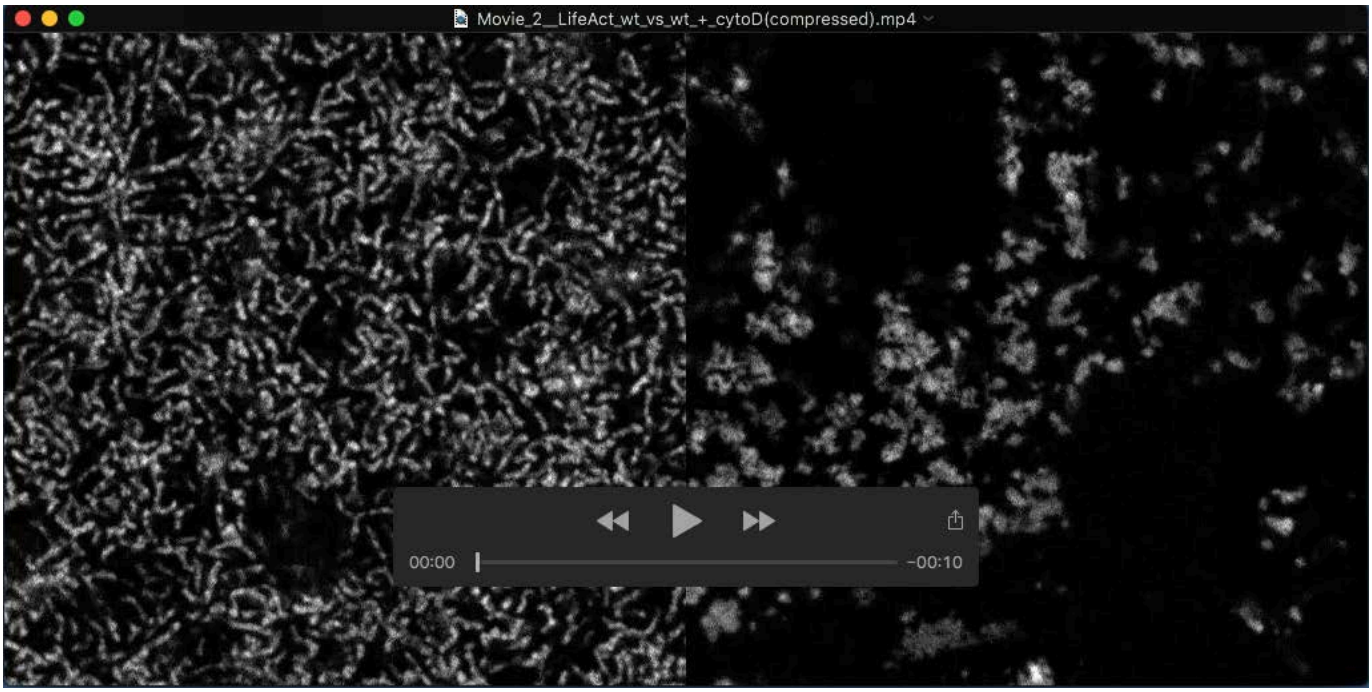

Movie 2. Cortical F-actin in live embryos: effect of cytochalasin D in wild-type. Left: cortical F-actin in wild-type, as in Movie 1 (left) and corresponding to still data in Fig. 6A. Right: F-actin cortex appears degraded, consistent with F-actin depolymerization. Representative movie of 3 trials. In both movies, F-actin is detected by the Life Act transgene, with images at 200x magnification, corresponding to scale bar in Fig. 6.

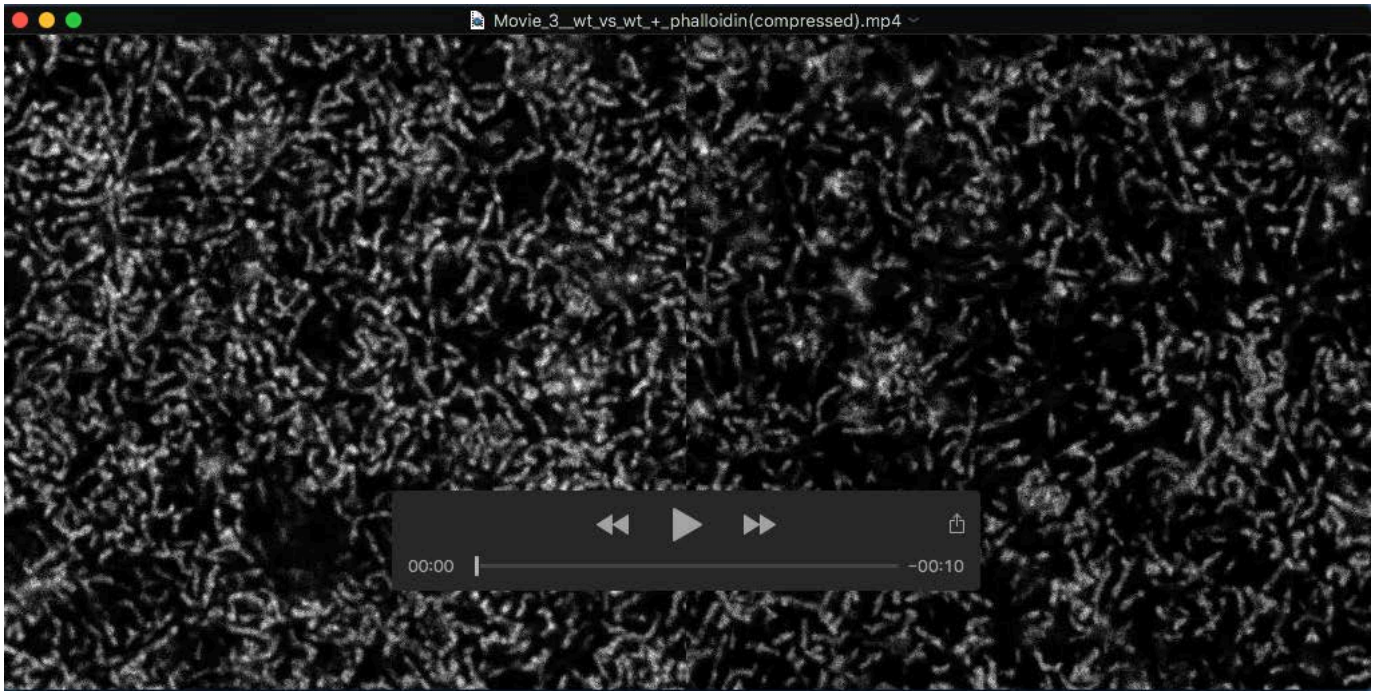

Movie 3. Cortical F-actin in live embryos: effect of phalloidin in wild-type. Left: cortical F-actin in wild-type, as in Movie 1 (left) and corresponding to still data in Fig. 6A. Right: F-actin dynamic movements are present. Representative movie of 2 trials. Apparently wider oscillations of the cortex compared to untreated embryos are observed in both movies. In both movies, F-actin is detected by the Life Act transgene, with images at 200x magnification, corresponding to scale bar in Fig. 6.

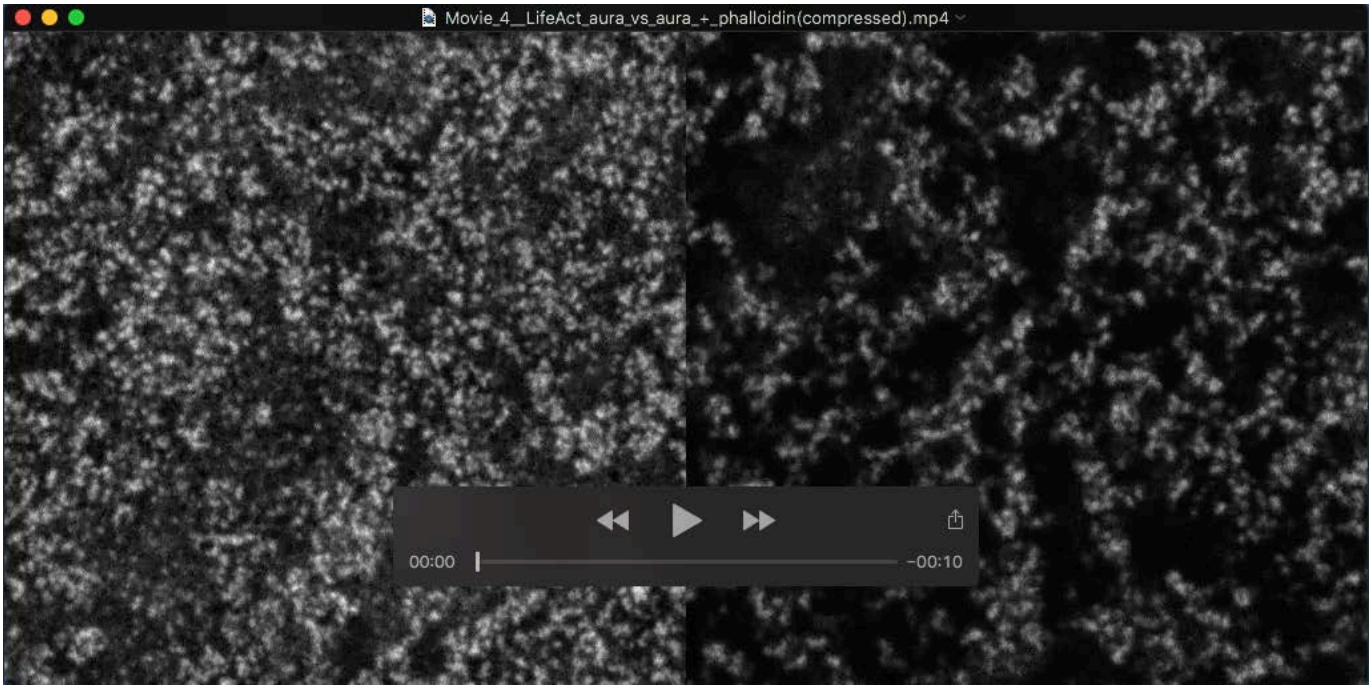

Movie 4. Cortical F-actin in live embryos: partial rescue of F-actin dynamics in *aura* mutants by phalloidin treatment. Left: cortical F-actin in *aura* mutants, as in Movie 1 (right) and corresponding to still data in Fig. 6B. F-actin dynamics defects characteristic or *aura* mutants are partially restored, as manifested by local cortical contractions and expansions. Representative movie of 3 trials. In both movies, F-actin is detected by the Life Act transgene, with images at 200x magnification, corresponding to scale bar in Fig. 6.

Supplementary Data

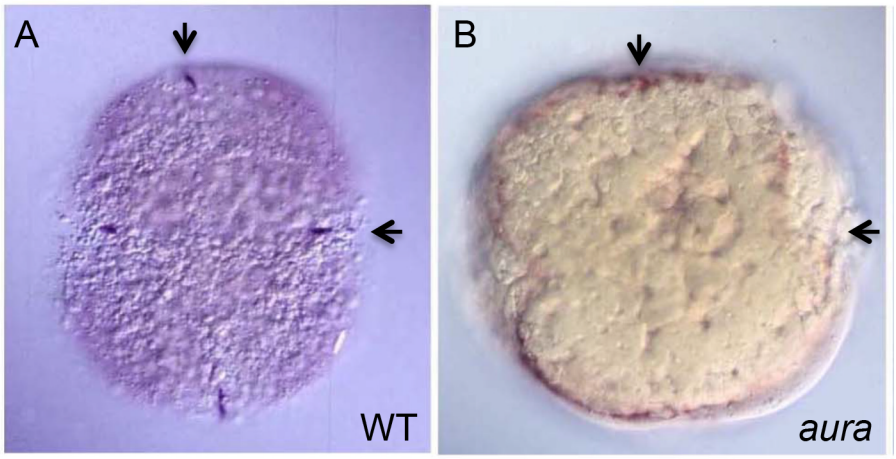

Figure S1: *vasa* RNA localization in *aura* mutant embryos. 4-cell stage embryos showing normal RNA furrow localization in wild-type (A) and reduced furrow localization and increase marginal enrichment in *aura* mutants (B). *vasa* RNA visualized as in Fig. 2A,B but using DAB (blue) visible substrate. Arrows show cleavage planes.

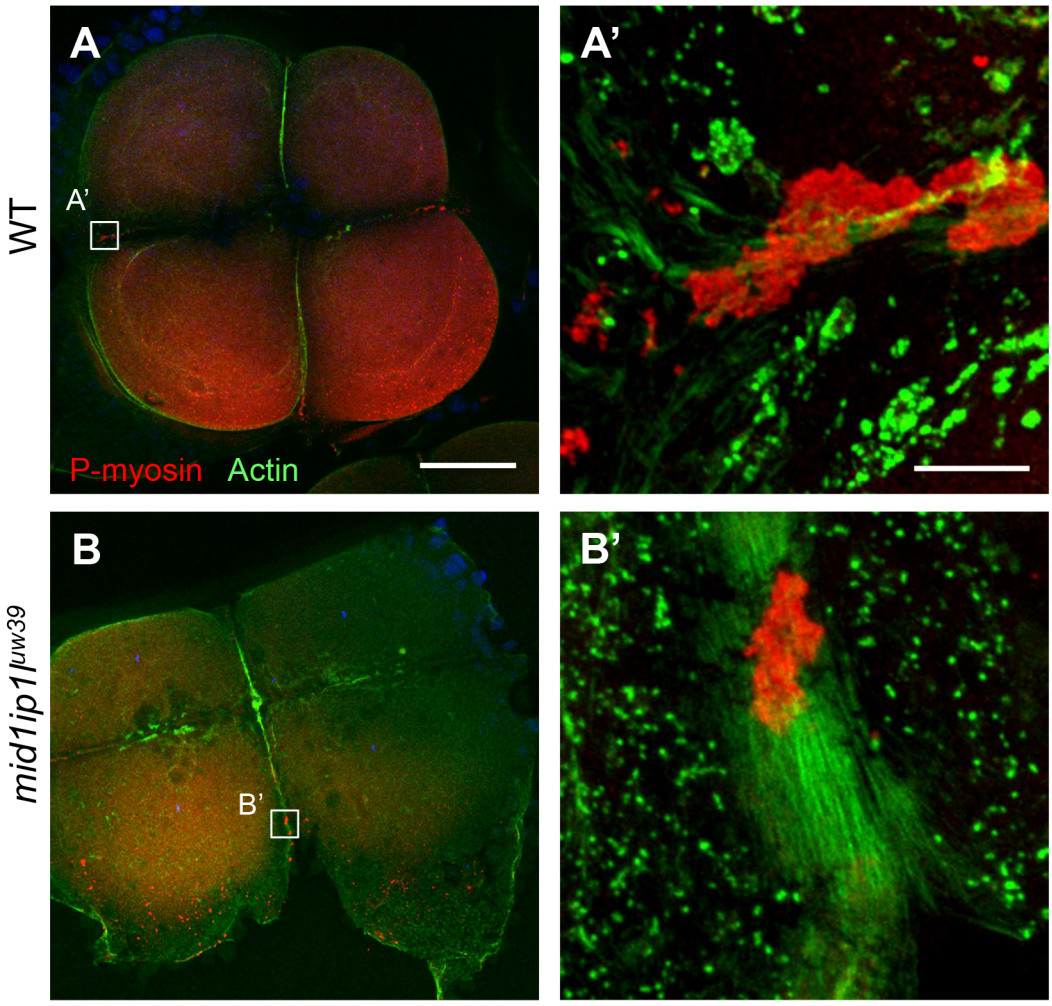

Figure S2: Maternal-effect germ plasm segregation defect in mutants for *mid1ip1l*^{uw39}. Localization of RNPs (using an anti-P-myosin antibody) and F-actin in wild-type (A, A') and embryos from females homozygous for the *mid1ip1l*^{uw39} alllele (B,B'). Scale: 100 µM A-D (bar in A), 10 µM A',B' (bar in A').

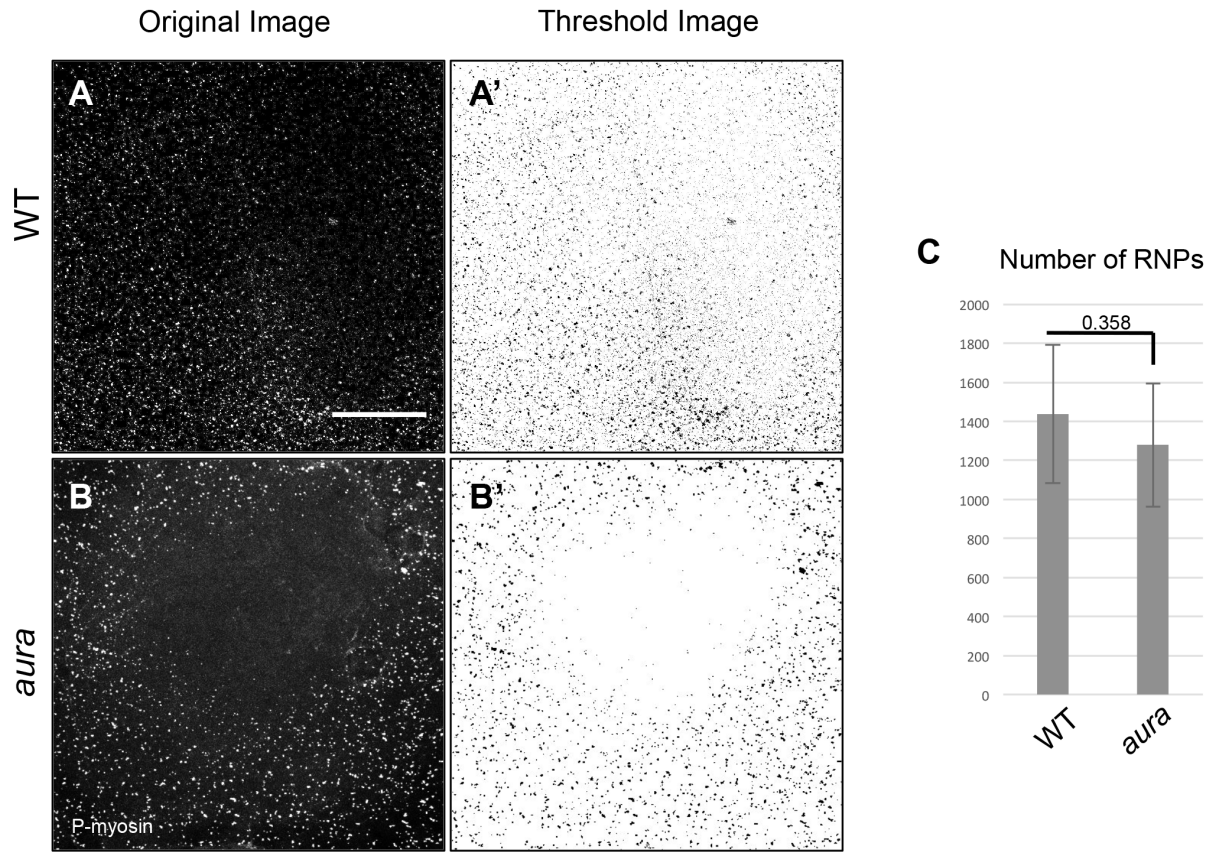

Figure S3: *aura* mutant embryos exhibit a similar initial number of cortical germ plasm RNPs. Wild-type and *aura* mutant embryos fixed at 12 mpf show a similar number of RNPs. (A.B) Labeling of RNP with anti-P-myosin. (A',B') Reversed grayscale for improved visualization. The RNP zone in the center of the blastodisc is likely the incipient zone of RNP clearing, which our observations suggest moves outward faster in *aura* mutants than in wild-type. (C) Quantification of the number of spots in image fields using automated particle counting (FIJI) shows no statistically significant difference between wild-type and mutant embryos (8 embryos each). Scale: 100 μM.

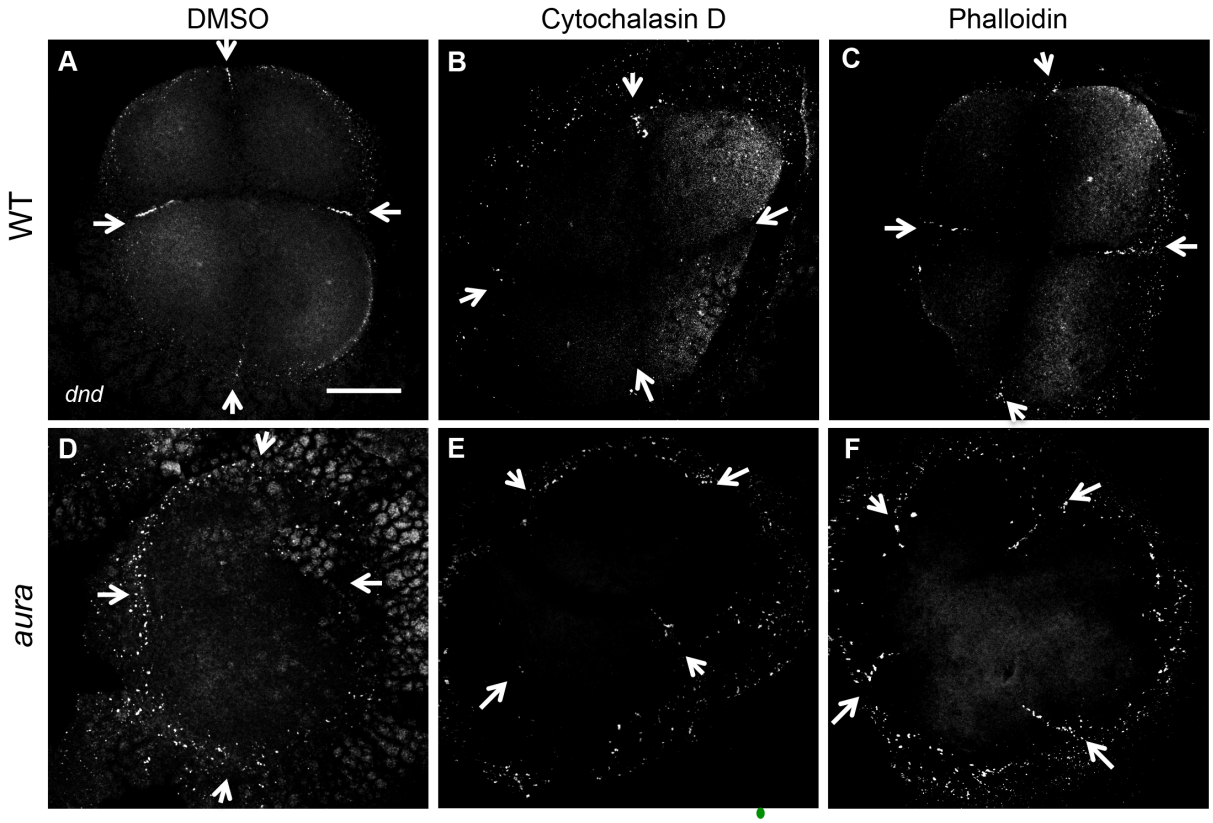

Figure S4: Effects of cytoskeletal inhibitors on germ plasm RNP furrow recruitment.
Fluorescent in situ hybridization to visualize *dnd* RNA localization. Scale: 100 µM A-F (bar in A)

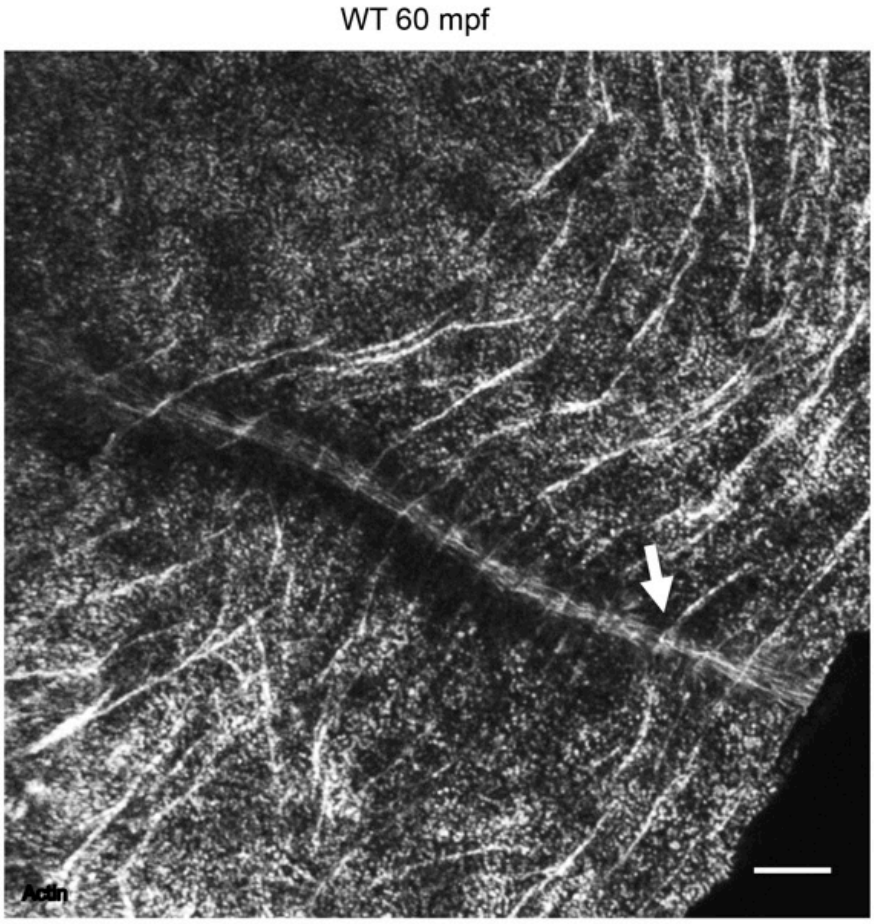

Figure S5: F-actin cortical trenches converge with F-actin furrow indentations. Overview of a wild-type embryo labeled for F-actin, showing that many circumferential F-actin arcs, which correspond to cortical trenches (Fig. 7A), connect to F-actin enrichments at the furrow (Fig. 7B), which correspond to furrow indentations.

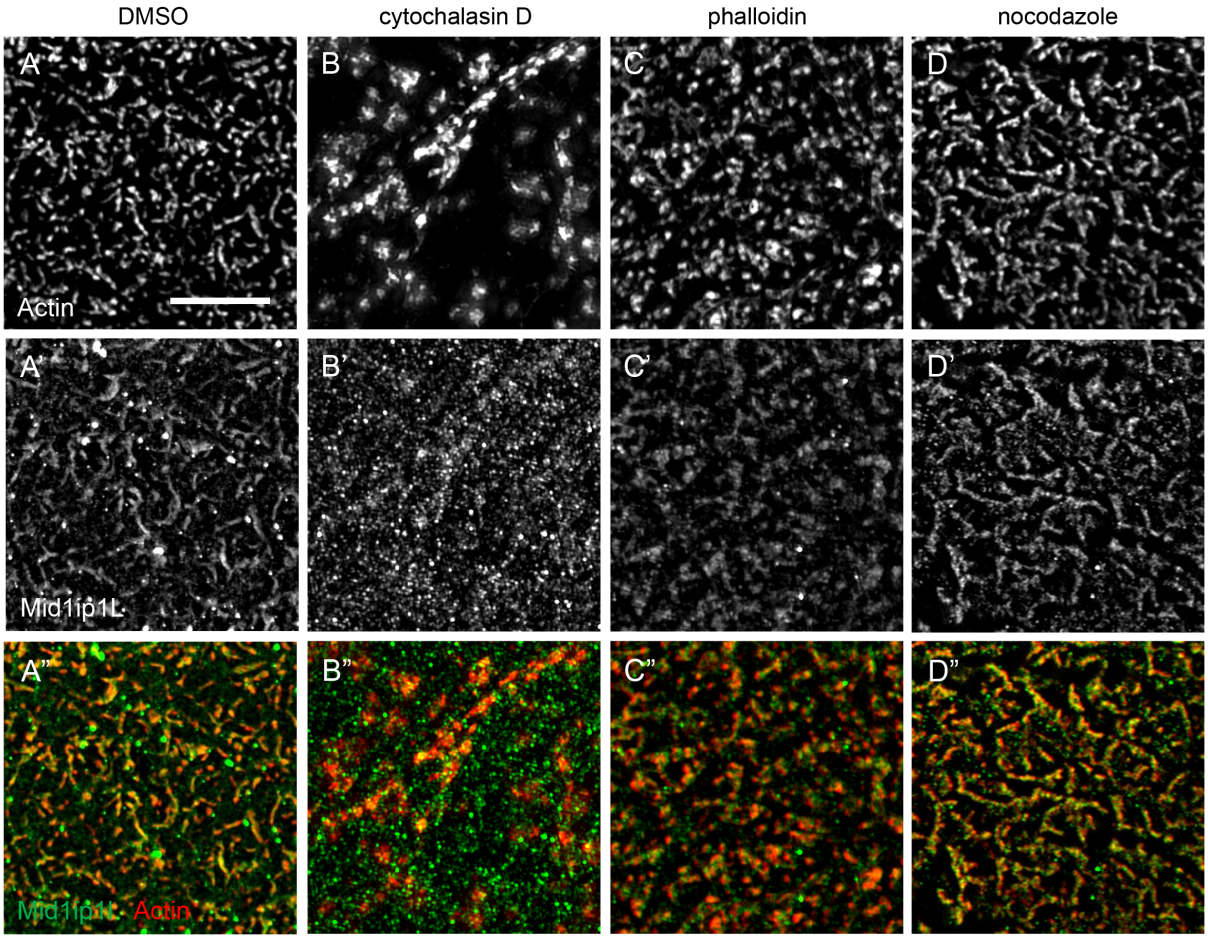

Figure S6: Mid1ip1L protein localization depends on F-actin, but not microtubules. SIM images showing localization of Mid1ip1l with respect to F-actin in the presence of cytoskeletal inhibitors. Both actin inhibition (B-B") and stabilization (C-C") lead to a reduction in colocalization. Colocalization appears unaffected by microtubule inhibition (D-D"). Scale: 5 μM A-H (bar in A).

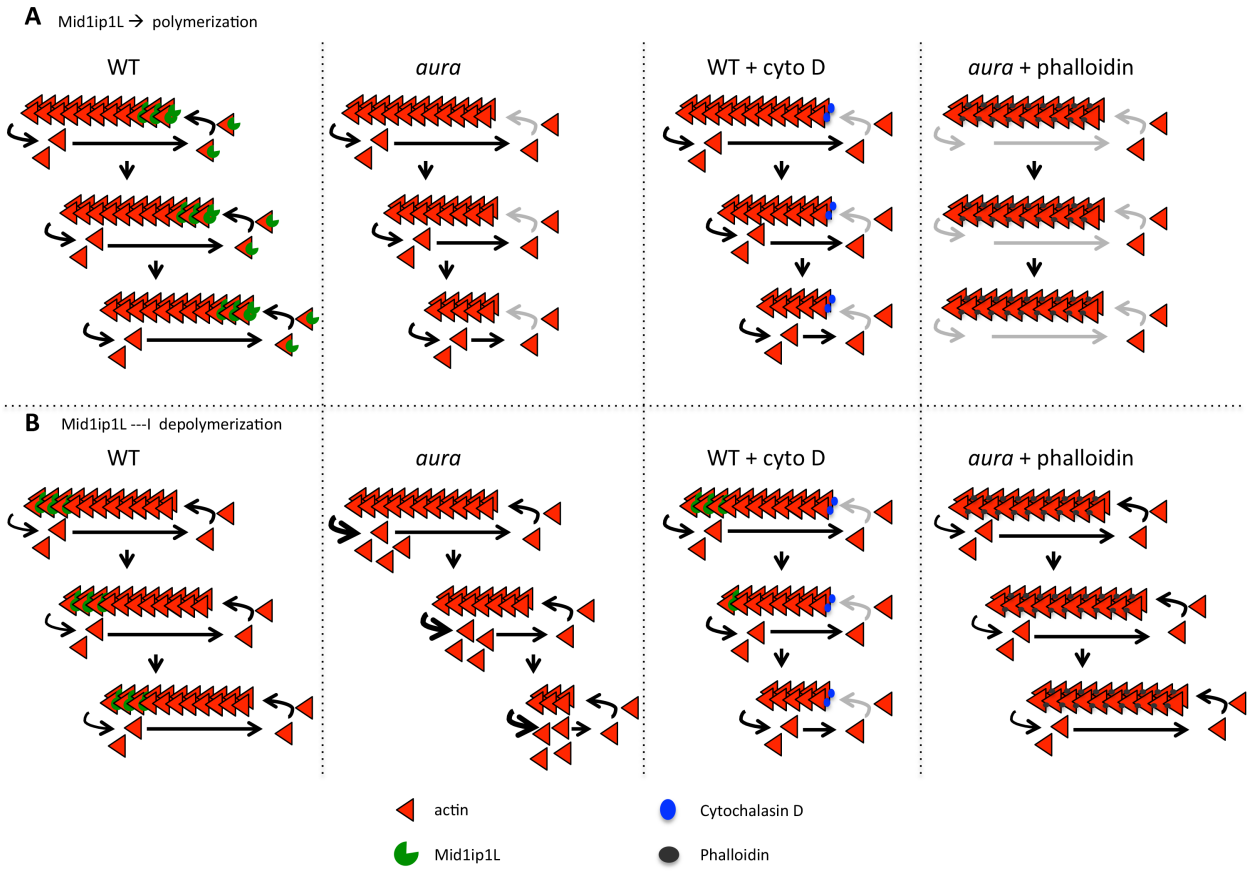

Figure S7: Potential mechanisms by which Mid1ip1L may regulate actin dynamics, and relation to inhibitor effects. Models based on the observed binding of Mid1ip1L to one end of short F-actin (Fig. 9), and effects of the cytochalasin D and phalloidin on the *aura* phenotype. A) Mid1ip1L promotes F-actin polymerization at the site of actin monomer addition (plus ends), so that reduced function results in decreased polymerization. B) Mid1ip1L downregulates the rate of F-actin depolymerization at the minus ends, so that the reduced function results in increased F-actin depolymerization. In both models, both *aura* mutants and cytochalasin D-treated wild-type embryos exhibit F-actin loss. In both models, stabilization of F-actin with phalloidin reduces the rate F-actin loss, allowing for the formation of short F-actin and partially rescuing the phenotype. Plus (barbed) end are shown on right and minus (pointed) ends on left, with F-actin treadmilling indicated by growth to the right from top (early in sequence) to bottom (later in sequence).

Table S1. Primers used for end-point genotyping.

Primer Name	5'-> 3'	Use
mid1ip1L Forward	TATCACCTCCACGGACTCTT	genotyping
mid1ip1L Reverse	CCGCCGATTTCTCTCTTGT	genotyping
mid1ip1L MUT Probe	/56FAM/TGT +C+C+T +AA+C +TAA C/3IABkFQ/	genotyping
mid1ipL WT Probe	/5HEX/TGT +C+C+A +AA+C T+AA CA/3IABkFQ/	genotyping

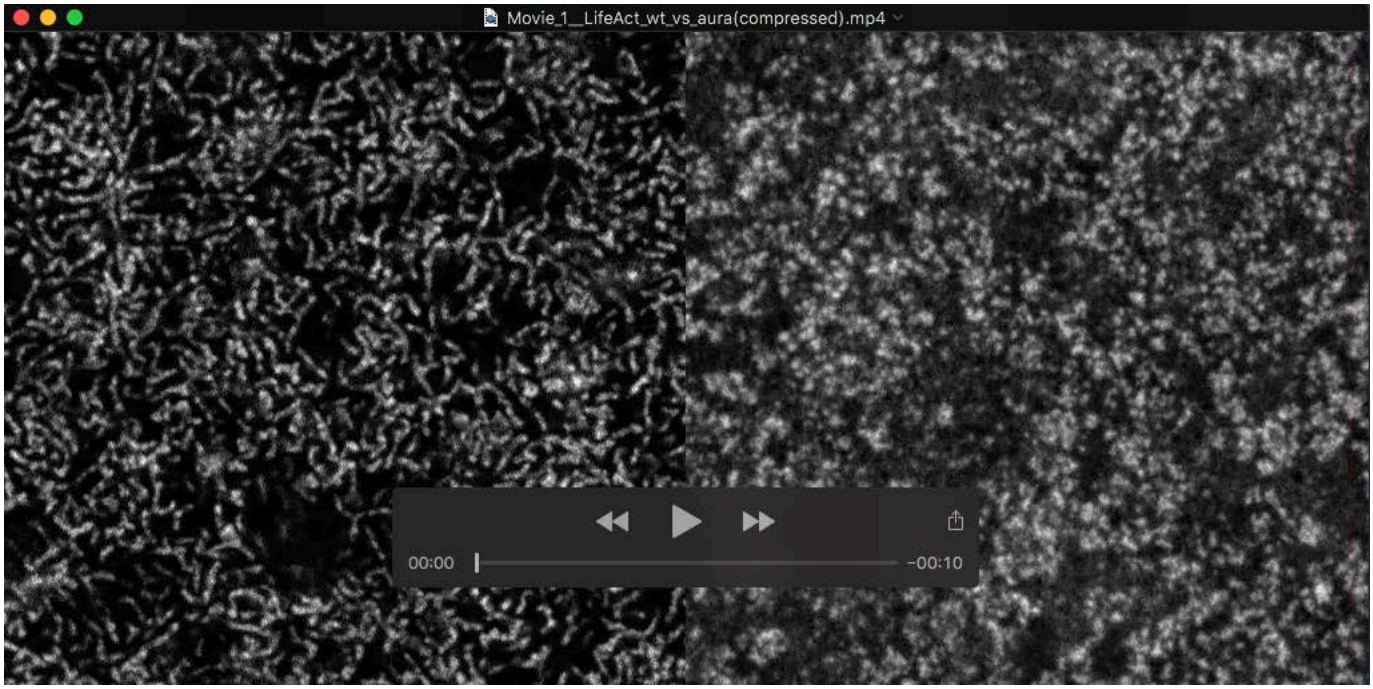

Movie 1. Cortical F-actin in live embryos: wild-type vs *aura* mutants. Left: In wild-type, cortical F-actin exhibits dynamic cyclical changes and local undulations. Movie corresponds to still data in Fig. 6A. Representative movie of 10 trials. Right: In *aura* mutants, cortical F-actin appears static and exhibits an aberrant reorganization. Movie corresponds to still data in Fig. 6B. Representative movie of 10 trials. In both movies, F-actin is detected by the Life Act transgene, with images at 200x magnification, corresponding to scale bar in Fig. 6.

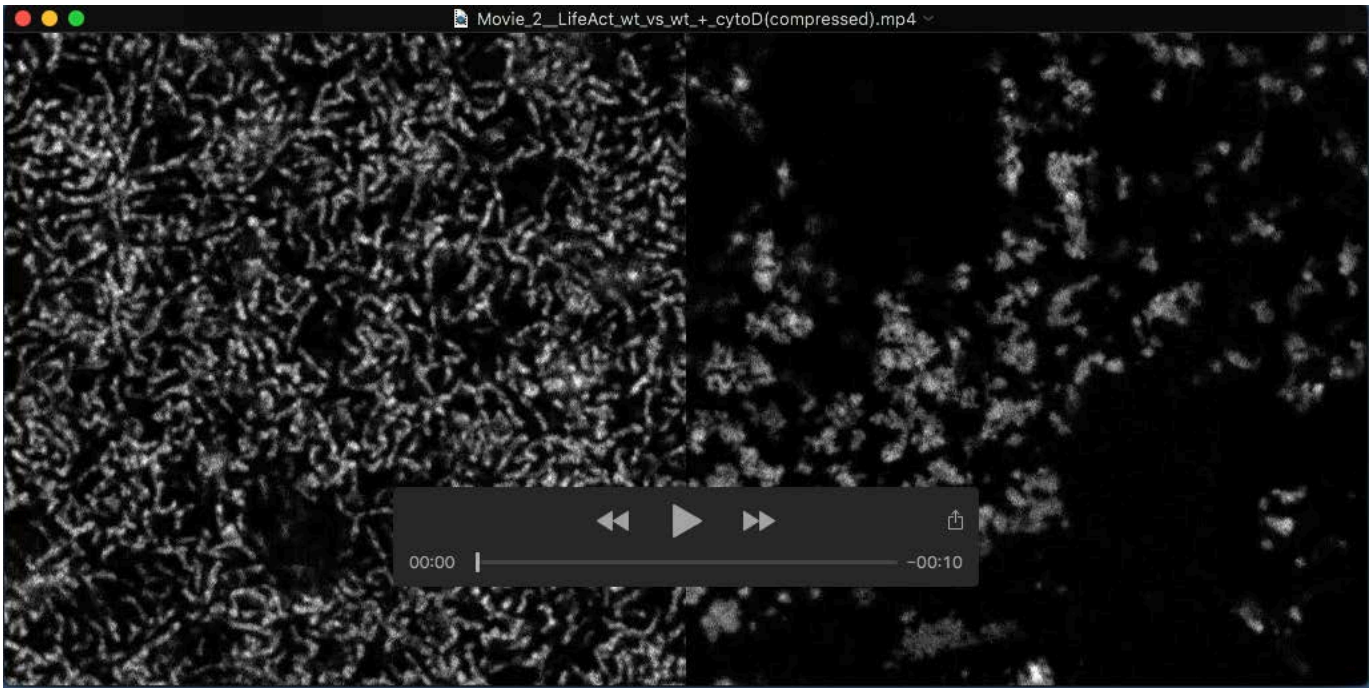

Movie 2. Cortical F-actin in live embryos: effect of cytochalasin D in wild-type. Left: cortical F-actin in wild-type, as in Movie 1 (left) and corresponding to still data in Fig. 6A. Right: F-actin cortex appears degraded, consistent with F-actin depolymerization. Representative movie of 3 trials. In both movies, F-actin is detected by the Life Act transgene, with images at 200x magnification, corresponding to scale bar in Fig. 6.

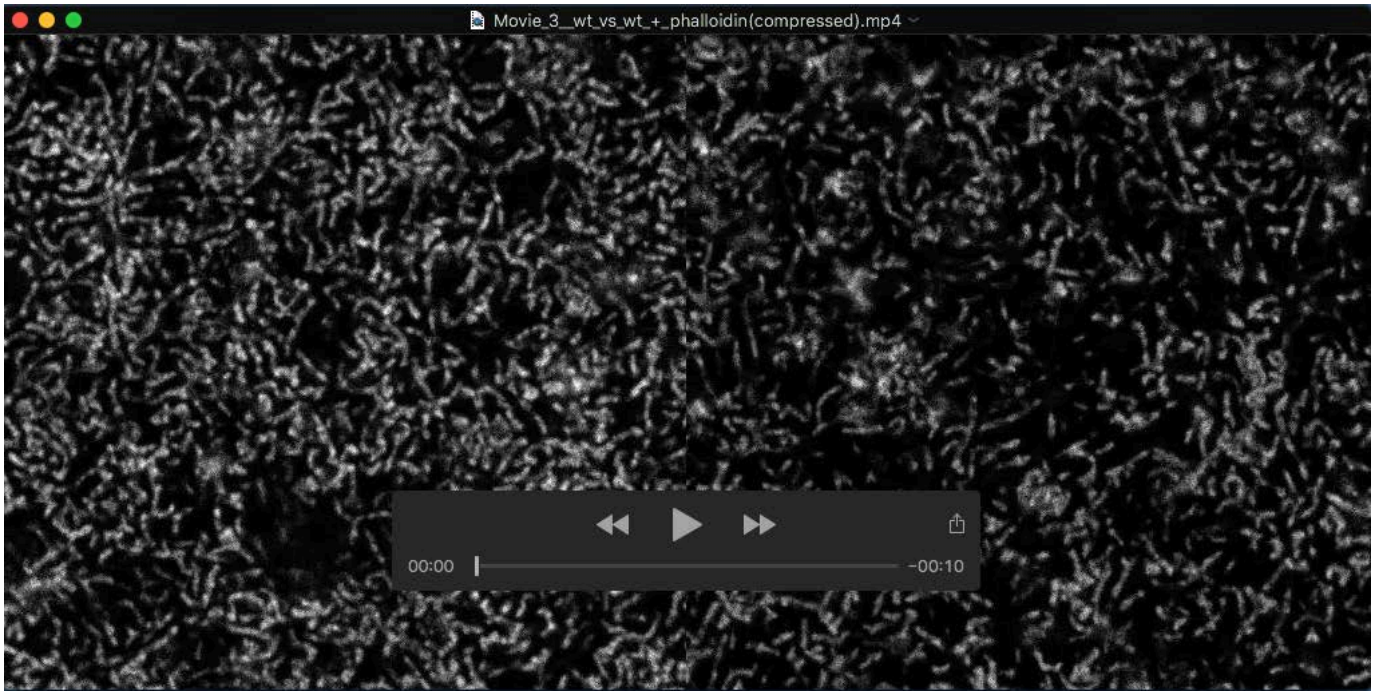

Movie 3. Cortical F-actin in live embryos: effect of phalloidin in wild-type. Left: cortical F-actin in wild-type, as in Movie 1 (left) and corresponding to still data in Fig. 6A. Right: F-actin dynamic movements are present. Representative movie of 2 trials. Apparently wider oscillations of the cortex compared to untreated embryos are observed in both movies. In both movies, F-actin is detected by the Life Act transgene, with images at 200x magnification, corresponding to scale bar in Fig. 6.

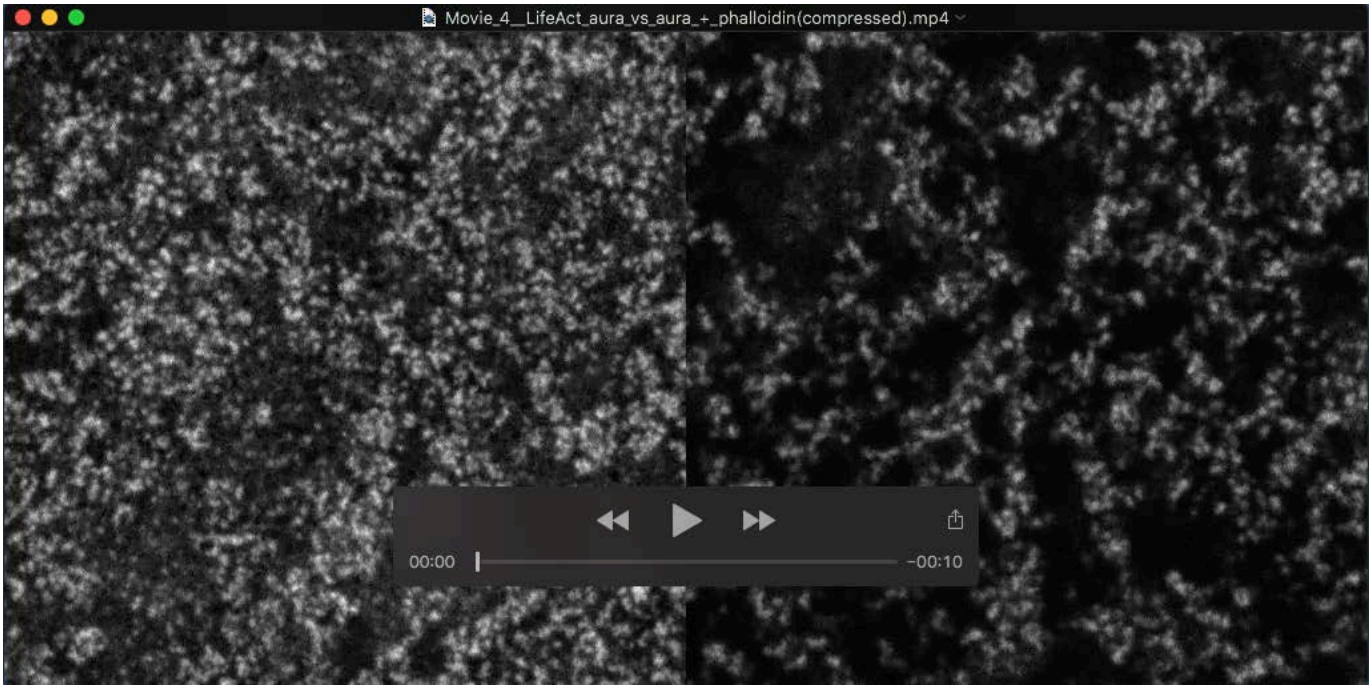

Movie 4. Cortical F-actin in live embryos: partial rescue of F-actin dynamics in *aura* mutants by phalloidin treatment. Left: cortical F-actin in *aura* mutants, as in Movie 1 (right) and corresponding to still data in Fig. 6B. F-actin dynamics defects characteristic or *aura* mutants are partially restored, as manifested by local cortical contractions and expansions. Representative movie of 3 trials. In both movies, F-actin is detected by the Life Act transgene, with images at 200x magnification, corresponding to scale bar in Fig. 6.